Excited State Molecular Dynamics: Beyond the Born-Oppenheimer Approximation

David B. Lingerfelt

A dissertation
submitted in partial fulfillment of the
requirements for the degree of

Doctor of Philosophy

University of Washington

2017

Reading Committee:

Xiaosong Li, Chair

Anne McCoy

Munira Khalil

Program Authorized to Offer Degree:
Chemistry Department

University of Washington

Abstract

Excited State Molecular Dynamics: Beyond the Born-Oppenheimer Approximation

David B. Lingerfelt

Chair of the Supervisory Committee:
Professor of Chemistry Xiaosong Li
Chemistry Department

Herein, numerical approaches for describing the time evolution of molecular systems in non-equilibrium, and excited electronic states using the tools of non-adiabatic molecular dynamics will be built up from the full molecular Hamiltonian and associated quantum mechanical equation of motion. This common formalism, from which all of the approximate methods emerge, is first presented in detail. The working equations for these methods, which are found to naturally arise from successive approximations to the quantum mechanical treatment of all molecular degrees of freedom, and presented along with details of their implementations in electronic structure programs utilizing atom-centered basis sets. Specific scientific studies and methodological developments relying on the resulting methods are then presented to highlight the utility of the developments. A central theme throughout this document will be to exploit the disparate timescales on which the heavy and light particles comprising molecular systems evolve through the combination of explicitly time dependent methods (in a mixed quantum-classical framework), and the tools of time-dependent perturbation theory to extract the temporal evolution of molecular systems in far-from-equilibrium conditions.

TABLE OF CONTENTS

LIST OF FIGURES

ACKNOWLEDGMENTS

The author wishes to express sincere appreciation to University of Washington Chemistry Department for the opportunity to pursue his passion for chemical dynamics, and for the unwavering support from his research advisor, Prof. Xiaosong Li, along the way.

DEDICATION

To my ever-patient and loving wife, Megan. Without her encouragement, I surely could never have realized the work detailed here.

Chapter 1

INTRODUCTION TO MIXED QUANTUM CLASSICAL MOLECULAR SIMULATION METHODS

1.1 The Molecular Hamiltonian and Quantum Equation of Motion

The prediction of molecular systems' time evolution from first principles provides a means to study fundamental chemical processes with spatial and temporal resolution unparalleled by most experiments.[4–6] Time-domain simulations of chemical systems can, for example, be used to reproduce absorption spectra with realistically broadened line-shapes[7–10], resolve mechanisms of complex chemical transformations[11,12], and obtain rate constants for non-equilibrium processes[13,14]. The exact chemical dynamics (in the non-relativistic limit at least) are well-known to result from integration of the time-dependent Schrödinger equation (TDSE, Eq. (1.1)).

$$i\dot{\Psi}(\mathbf{R},\mathbf{r};t) = \mathscr{H}(\mathbf{R},\mathbf{r};t)\,\Psi(\mathbf{R},\mathbf{r};t) \tag{1.1}$$

$\mathscr{H}$, the molecular Hamiltonian, is the generator of time translations for the molecular wave function Ψ, which depends explicitly on nuclear and electronic degrees of freedom (DOF) $\mathbf{R}$ and $\mathbf{r}$, and parametrically on time, t. The molecular Hamiltonian expressed in the atomic unit system (used throughout this document unless otherwise noted) is given in Eq. (1.2).

$$\begin{aligned} \mathscr{H} &= -\sum_a \tfrac{1}{2M_a}\nabla^2_{\mathbf{R}_a} - \sum_b \tfrac{1}{2}\nabla^2_{\mathbf{r}_b} + V(\mathbf{r},\mathbf{R}) \\ &= -\sum_a \tfrac{1}{2M_a}\nabla^2_{\mathbf{R}_a} + \mathscr{H}_r(\mathbf{r},\mathbf{R}) \end{aligned} \tag{1.2}$$

Here, a and b index the nuclear and electronic DOF respectively, M_a is the mass of nuclei a, and $V(\mathbf{r},\mathbf{R})$ is the total potential energy operator collecting all electrostatic interaction terms between electrons and nuclei. Eigenfunctions of the last two terms in Eq. (1.2) (i.e. the functions $\{\Phi_i\}$ which are solutions of the time-*independent* electronic Schrödinger equation, $\mathscr{H}_r(\mathbf{r},\mathbf{R})\Phi_i(\mathbf{r};\mathbf{R}) = E_i(\mathbf{R})\Phi_i(\mathbf{r};\mathbf{R})$), form a complete basis at each $\mathbf{R}$ in which Ψ may be expanded. Similarly resolving the nuclear wave functions associated with each Φ_i in their energy eigenbasis requires *a priori* knowledge of global electronic potential energy surfaces

(PES's), i.e. eigenvalues of $\mathscr{H}_r(\mathbf{r},\mathbf{R})$ for all $\mathbf{R}$ where the nuclear wave function is non-zero.[15–17] Nonclassical nuclear phenomena such as tunneling and zero-point energy formally mandate treatment in terms of the quantized nuclear energy levels. For heavier nuclei at moderately high temperatures, though, these effects are negligible and treating the nuclei classically and electrons quantum mechanically is only a mild approximation. These "mixed quantum-classical" (MQC) formalisms[18–20] offer favorable compromise between accuracy and computational expense in this case, and the system can be selectively partitioned to allow a subset of nuclear DOF to be treated quantum mechanically.[14,21]

1.2 Overview of Mixed Quantum-Classical Molecular Dynamics Approaches

This simplest of the MQC methods neglects the exciton-phonon coupling altogether, under the assumption that electronic eigenstates are well separated relative to the nuclear kinetic energy (i.e. the Massey parameter < 1)[22–24] This approach is commonly referred to as "Born-Oppenheimer molecular dynamics". In this situation, electronically adiabatic time evolution for the molecular system is enforced. If the nuclear dynamics brings the system to a point in the configuration space where two (or more) electronic energy eigenstates become degenerate, or nearly so, electronic non-adiabaticity can play a dominate role in determining the dynamics, and the effect which slow particle motions exert on the fast particles evolution (and *vice versa*) must be accounted for.

To describe the molecular dynamics in the case where two or more electronic energy surface are strongly coupled through the nuclear motions, the electronic wave function can be allowed to evolve into a superposition of eigenstates which mix according to the non-diagonality of the nuclear kinetic energy operator in the electronic energy eigenbasis. The enormous complication that results from relaxing the electronic adiabaticity constraint is that nuclear dynamic are no longer strictly amenable to a classical treatment. Components of the superposition associated with excited electronic states would exhibit proportionately lower nuclear momenta, inevitably leading to a non-local nuclear wave function over time. One approximation to circumvent this dilemma is to let the nuclei experience the expectation value of the force evaluated for the electronic superposition. In this way, the nuclei experience the "mean field" forces of the vibrationally-coupled electronic states; an approach often referred to as Ehrenfest dynamics. The nuclear delocalization problem is avoided at the cost of foregoing dynamical electron-nuclear correlations in this framework. This shortcoming causes a lack of microscopic reversibility and, therefore, detailed balance[25] that leads to spurious energy transfer from the slow to fast DOF.[26,27] Even still, short-time dynamics of systems exhibiting significant non-adiabatic coupling are often well-approximated with the Ehrenfest approach, and detailed balance can be artificially restored somewhat though application of thermostats[21] or by externally reintroducing electron-nuclear dynamical correlation back into the propagated state.[28,29]

Multi-configurational mixed quantum-classical approaches (e.g. Multiple Spawning[30], Ring Polymer[31,32]/Centroid[33] MD, etc) capture correlations in the fast and slow DOF, but scale less favorably than the mean field approach due to increased dimensionality of their molecular wave function *ansatz*. The performance and expense of these multi-configurational techniques is well-document in the literature.[34–36] Independent trajectory surface-hopping (TSH) approaches have been introduced in an effort to decouple the evolution of nuclear wave functions associated with different electronic states,[37,38] and often produce results that align favorably with experiment and full quantum dynamics simulations.[39–41] Swarms of independent TSH trajectories offer a stochastic sampling of the dynamical electron-nuclear correlation neglected by the mean field dynamics. Since TSH permits deviation of the nuclear trajectories from the majority probability time-evolution channel, it is better suited for exploring dynamics initiated by rare events than the Ehrenfest scheme. These minority probability nuclear evolution channels are important to the dynamics of systems undergoing, e.g., photochemical processes and high-energy molecular collisions.

While there are numerous implementations of TSH dynamics intended for use alongside electronic structure theory packages[39,40,42–46] most of the previous works resort to making computational affordable approximations for: the excited state potential energy surfaces, treatment of the quantum "back-reaction" describing the effect electronic transitions exert on the nuclear evolution, and/or evaluation of the non-adiabatic couplings. With the recent derivations of analytical derivative couplings for low-scaling, single-reference electronic structure formalisms$^{47–52}$ and ever-increasing computational power, it becomes possible to carry out first-principles on-the-fly surface-hopping dynamics.

1.3 Derivations of the Canonical Mixed Quantum-Classical Simulation Methods

To arrive at a method capable of capturing the dynamical correlations between electronic and nuclear DOF, a multi-configuration *ansatz* for the molecular wave function is first posited:

$$\Psi(\mathbf{R},\mathbf{r},t) = \sum_k \Omega_k(\mathbf{R},t)\Phi_k(\mathbf{r},\mathbf{R}) \tag{1.3}$$

Here, we have associated a many-body nuclear wave function, Ω_k, with each electronic adiabat, Φ_k, where a complex exponential "phase factor" between the electronic and nuclear wave functions has been implicitly absorbed into each Ω_k. Substituting this ansatz into Eq. (1.1), multiplying on the left by $\Phi_j^*(\mathbf{r},\mathbf{R})$, and integrating over $\mathbf{r}$ yields the Schrödinger equation for the nuclear wave functions:

$$\begin{aligned} i\frac{\partial\Omega_k(\mathbf{R},\mathbf{t})}{\partial t} &= -\sum_a \tfrac{1}{2M_a}\nabla^2_{\mathbf{R}_a}\Omega_k(\mathbf{R},t) + E_k(\mathbf{R})\Omega_k(\mathbf{R},t) \\ &+ \sum_{a,j}\left(\tfrac{1}{2M_a}D^a_{kj}\Omega_j(\mathbf{R},t) - \tfrac{1}{M_a}d^a_{kj}\cdot\frac{\partial\Omega_j(\mathbf{R},t)}{\partial\mathbf{R}_a}\right) \end{aligned} \tag{1.4}$$

where we've made the following definitions:

$$d^a_{kj} = \langle\Phi_k|\,\partial\Phi_j/\partial\mathbf{R}_a\rangle \tag{1.5}$$

$$D^a_{kj} = \left\langle\Phi_k|\partial^2\Phi_j/\partial\mathbf{R}_a^2\right\rangle \tag{1.6}$$

From Eq. (1.4), a physical picture for the nuclear evolution emerges. Piecewise application of Ehrenfest's theorem to the first two terms in Eq. (1.4) gives the centers of the k^{th}

nuclear wave function evolving according to the curvature of the corresponding adiabatic PES. The third term contains the second derivative couplings, D_{kj}, which contribute small corrections to the adiabatic nuclear kinetic energies and inter-state couplings that are generally safe to neglect in this context.[53] The final term in Eq. (1.4) is primarily responsible for the changes in the composition of the electronic superposition brought about by the nuclear momentum operator evaluated between adiabats, d_{kj}. The effect of these terms on the molecular evolution is what one strives to account for through the application of non-adiabatic approaches to molecular dynamics.

Since the goal is to arrive at a classical trajectory-based method, we promptly take the classical limit for the nuclear DOF by identifying each nuclear wave function with a (Hartree) product of Dirac delta functions, $\delta(\mathbf{R} - \mathbf{R}_k(t))$, centered on the nuclei:

$$\Omega_i(\mathbf{R}, \mathbf{R}_k(t)) = c_k(t)\,\delta(\mathbf{R} - \mathbf{R}_k(t)) \tag{1.7}$$

The complex coefficients $\{c_k(t)\}$ collect the weights and phases for each product $(\Omega_k \cdot \Phi_k)$ contributing to the superposition state and $\mathbf{R}_k(t)$ gives the coordinates of the classical nuclei evolving according to the forces from the k^{th} adiabatic state. Note that $\langle \Phi_k | \dot{\Phi}_j \rangle = \dot{\mathbf{R}}_j(t) \cdot \langle \Phi_k | \nabla_{\mathbf{R}_j} | \Phi_j \rangle$ in the absence of any external time-dependent potential. Substituting the "classical nuclei" wave function ansatz for Ω (Eq. (1.7)) back into the TDSE (Eq. (1.1)) gives, with some straight-forward algebraic manipulations and neglecting the second derivative couplings, the equation of motion for $c_k(t)$:

$$\begin{aligned} i\dot{c}_k(t) &= \sum_j \underbrace{\left(\delta_{kj}\mathbf{V}_{jj} - i\dot{\mathbf{R}}_j(t) \cdot \mathbf{d}_{kj}\right)}_{\mathbf{H}_{kj}} c_j(t) \\ &= \sum_j \mathbf{H}_{kj} c_j(t), \end{aligned} \tag{1.8}$$

where $\mathbf{V}_{kj} = \langle \Phi_k | \mathscr{H}_r | \Phi_j \rangle$. Since we choose to work in the adiabatic basis, $\{\Phi_j\}$ are eigenfunctions of the electronic Hamiltonian and $\mathbf{V}$ becomes diagonal. Ehrenfest's theorem gives the time-dependence for the nuclear position and momentum expectation values equivalent to the Newtonian equation of motion (Eq. (3.4).)

$$-\frac{\partial \mathbf{V}_{jj}}{\partial \mathbf{R}_j} = \mathbf{m}\ddot{\mathbf{R}}_\mathbf{j} \tag{1.9}$$

So, by taking the classical limit for the nuclear wave function associated with each electronic adiabat in the multi-configuration wave function, we have arrived at a trajectory based method *of sorts*, where the non-adiabatic coupling between electronic energy eigenstates mixes the "classical" trajectories. Admitting the possibility of electronic non-adiabaticity folds some uncertainty back into the nuclear positions, and the equations of motion we arrive at describe a delocalized superposition of otherwise sharply localized nuclear wavefunctions. The centers of the nuclear wave functions, $\{\mathbf{R}_k\}$, spread according to the disparate forces they encounter along their respective electronic PES's. As a result, even if the system is initially prepared in an eigenstate of the nuclear position operator, it may not remain so as the nuclei move. Instead, $c_k(t)c_k(t)^*$ gives the probability of observing the system in the k^{th} nuclear position eigenstate at time t. More generally, $\rho_{jk}(t) = c_j(t)c_k^*(t)$ are elements of the one-particle reduced density matrix.[54] The notion of classical nuclei acting as observers of the quantum electronic state as they evolve has been explored in some recent non-TSH developments in the field of non-adiabatic dynamics.[55]

From this vantage, the mean-field, Ehrenfest molecular dynamics approach can be easily defined. Rather than allowing each of the nuclear wavefunctions, $\delta(\mathbf{R} - \mathbf{R}_j)$, in Eq. (1.7) to evolve independently of one another according to the particular forces evaluated at $\mathbf{R} = \mathbf{R}_j$, the locality of the nuclei can be preserved while at the same time accounting, on average, for the non-adiabatic electronic evolution by equating the forces on the nuclei to the expectation value of the forces evaluated for the time-evolving wave packet (Eq. (1.10).)

$$-\langle \nabla_R \mathbf{V} \rangle = \mathbf{m}\ddot{\mathbf{R}}_\mathbf{j} \tag{1.10}$$

Furthermore, if the short-time behaviour of the electronic degrees of freedom in response to some perturbation is the only dynamical quantity of interest, the simulation can be further simplified by ignoring the vibrational dynamics altogether. Of course, this approach can only provide a meaningful result if the simulation length is sufficiently short relative to the characteristic timescale of the nuclear motions. By enforcing that the electronic degrees of freedom evolve in the presence of fixed nuclei, the terms that involve the nuclear velocities in Eq. (3.3) are zeroed out, and we recover the TD-SCF electronic equation of motion. Numerical integration of this simpler equation of motion for the electronic evolution only is referred to in the quantum chemistry literature as the "real-time" time dependent SCF method for electronic dynamics (to distinguish from the "TD-SCF" term that colloquially refers to the linear response, perturbation theory method for solving for excitation energies between electronic states as the poles of the TD-SCF linear response function.)

The state of the system is propagated by integrating the coupled set of differential equations (Eqs. (3.3) to (3.4), or some subset thereof) However, as the $\mathbf{R}_k$'s in Eq. (3.3) begin to delocalize, the matrix elements $\mathbf{d}_{jk}$ also become non-local, sharply increasing the cost of evaluating the dynamics.[56,57] For the sake of practicality, an "independent trajectory approximation" is invoked in which nuclear evolution on each electronic energy eigenstate is assumed identical, i.e. $\mathbf{R}_k(t) = \mathbf{R}_0(t)$ for all k. Electron-nuclear coherence is spuriously enforced in each trajectory under this approximation, and error is accrued in $\{c_k(t)\}$ since nuclear wave functions evolving on the different PES's should dephase from one another, diminishing (on average) their overlap.[58,59] The $\{c_k(t)\}$ from a given independent trajectory no longer individually represent the temporal behavior of the system. However, error in the independent trajectories' $\{c_k(t)\}$ can be partially removed by taking the population-weighted average of the $\{c_k(t)\}$ over all possible trajectories (started from the same initial conditions) that would result from at each instant in time allowing the nuclei evolve according to the forces of each adiabat.[60] It is easy to show that number of these speculative trajectories (i.e. answers to the question "if state i contributes the forces now, how would the nuclei move?" for all i) increases *factorially* in time. However, the most heavily weighted trajectories in the average can be preferentially sampled so that error in $\{c_k(t)\}$ can be minimized with sub-factorial time complexity.

With this idea in mind, the TSH algorithm can be straightforwardly motivated. In the TSH approach, nuclei evolve according to the curvature of a single adiabatic state's PES, with stochastic switches of the state that contributes the instantaneous forces ("surface-hoping") during each TSH trajectory.[38] At a given time, the probability of the system being observed in nuclear position eigenstate k (given by $|c_k(t)|^2$) determines the probability of the k^{th} state contributing the nuclear forces. In this way, a set (or 'swarm') of TSH trajectories recovers the branching statistics of bifurcating nuclear wave packet trajectories to account for the dynamic correlation between $\{c_k(t)\}$ and nuclear forces in each trajectory, while simultaneously ensuring that the average behavior of the nuclear dynamics across many trajectories is consistent with the average $\{c_k(t)\}$.

The probability of switching the state contributing the forces from k to j, which minimizes the number of switches[14,61] required to maintain average nuclear forces consistent with $\{c_k(t)\}$ across a swarm of trajectories, is given by:

$$g_{jk}(t+\Delta t_n) = \int_t^{t+\Delta t_n} dt' \, \frac{-2\mathbb{R}\mathrm{e}(c_k(t')c_j^*(t'))\,\dot{\mathbf{R}}_0(t')\cdot\mathbf{d}_{kj}(t')}{c_j(t')c_j^*(t')} \tag{1.11}$$

$g_{jk}(t)$ is compared to a uniformly distributed random number, η, on the open interval (0,1). If $g_{jk} \leq \eta$, no hop occurs and the numerical integration of Eqs. (3.3) to (3.4) continues with no change in the state contributing the nuclear forces. If $g_{jk} > \eta$, then the component of the nuclear momentum along d_{jk} is checked to ensure the nuclear kinetic energy along the coupling vector is greater or equal to the difference in potential energy of the two states. If so, the hop is accepted, nuclear momenta are rescaled to conserve total energy, and the forces that dictate the evolution of the nuclei in the next time step will be those of state k. Otherwise, the hop is rejected. Because classically forbidden hops are disallowed, the TSH approximately satisfies detailed balance and reproduces the Boltzmann distribution for electronic state populations at long times.[26] This strict energy conservation condition can also be relaxed somewhat according to the time-energy uncertainty relation to account for nuclear tunneling events that manifest as classically forbidden transitions.[62]

Chapter 2

TRAJECTORY SURFACE HOPPING DYNAMICS

In this chapter, a direct *ab initio* surface-hopping method is presented for studying non-radiative decay processes induced by electronic non-adiabaticity. Electronic energies, analytical forces and non-adiabatic couplings will be supplied by first principles calculations carried out "on-the-fly" along the nuclear trajectories. We also present an approach to expedite the acquisition of temporal properties of systems exhibiting non-adiabatic effects, relying on an external biasing procedure to accelerate the dynamics in a systematic, reproducible fashion. This approach will be referred to as the meta-surface-hopping method. The implementation outlined here uses the random phase approximation (RPA) with either a Hartree-Fock or density functional theory ground (reference) state to treat the many-body problem for excited electronic states,[63–74] accounts for the effect of electronic transitions on the nuclear dynamics, and makes use of analytical expressions for the non-adiabatic coupling between electronic states. Thus, our implementation is designed to capture all of the requisite physics to accurately predict electron-phonon scattering processes for general molecular and condensed-phase systems.

We begin by presenting the relevant details of the implementations of the trajectory surface hopping method, including working equations and pseudo-code for the numerical integration of the molecular equations of motion. We then introduce the meta-surface-hopping biasing scheme which combines the strengths of TSH and time-dependent perturbation theory to accelerate the evaluation of dynamical properties of electronically non-adiabatic systems. The developed concepts are then applied to a test case that expedites the calculation of non-radiative decay rates for a small photo-excited model system, and are statistically validated through application to the one-dimensional avoided crossing model problem of non-adiabatic dynamics.

2.1 Direct *Ab Initio* Surface-Hopping Algorithm using a Split Integrator

Since the characteristic timescales on which the electronic and nuclear DOF evolve differ by many orders of magnitude, split time-scale integration schemes can be safely applied to promote computational efficiency. In the following section, we describe our implementation of direct *ab initio* fewest switches TSH method in the development version of the Gaussian[75] suite of electronic structure programs with interface to the direct BOMD algorithm.[76,77] In the direct formalism, all components of the TSH method, including the potential energy, force and non-adiabatic coupling, are computed "on-the-fly".

In the current work, Eq. (3.4) is integrated numerically by the velocity Verlet algorithm:

$$\dot{\mathbf{R}}_{\mathbf{0}}(t+\tfrac{1}{2}\Delta t_n) = \dot{\mathbf{R}}_{\mathbf{0}}(t) + \frac{1}{2}\ddot{\mathbf{R}}_{\mathbf{0}}(t)\Delta t_n \tag{2.1a}$$

$$\mathbf{R}_{\mathbf{0}}(t+\Delta t_n) = \mathbf{R}_{\mathbf{0}}(t) + \dot{\mathbf{R}}_{\mathbf{0}}(t+\tfrac{1}{2}\Delta t_n) \tag{2.1b}$$

$$\dot{\mathbf{R}}_{\mathbf{0}}(t+\Delta t_n) = \dot{\mathbf{R}}_{\mathbf{0}}(t+\tfrac{1}{2}\Delta t_n) + \frac{1}{2}\ddot{\mathbf{R}}_{\mathbf{0}}(t+\Delta t_n)\Delta t_n \tag{2.1c}$$

with nuclear time step Δt_n.

Eq. (3.3) can equivalently be expressed in matrix/vector notation (Eq. (2.2)).

$$i\dot{\mathbf{c}}(t) = \mathbf{H}(t)\mathbf{c}(t). \tag{2.2}$$

The vector of complex coefficients, $\mathbf{c}(t)$, is propagated here using a midpoint unitary transformation method:[78,79]

$$\mathbf{c}(t+\Delta t_e) = \mathbf{U}\left(t+\frac{1}{2}\Delta t_e\right)\mathbf{c}(t) \tag{2.3}$$

$$\mathbf{U}(t) = \exp[-i\mathbf{H}(t)\Delta t_e] \tag{2.4}$$

where Δt_e is the electronic time step. The matrix exponentiation is carried out by first expressing $\mathbf{H}(t)$ in its eigenbasis:

$$\mathbf{H}(t) = \mathbf{\Lambda}(t)\,\epsilon(t)\,\mathbf{\Lambda}^{\dagger}(t) \tag{2.5}$$

Then the propagator can be easily constructed:

$$\mathbf{U}(t) = \mathbf{\Lambda}(t)\exp[-i\,\Delta t_e\,\epsilon(t)]\,\mathbf{\Lambda}^{\dagger}(t). \tag{2.6}$$

The hopping probabilities defined in Eq. (1.11) are conveniently evaluated by numerical integration with the same discrete time step utilized in the electronic propagation. At each step in the numerical integration of Eq. (3.3), the integrand of Eq. (1.11) is evaluated and multiplied by the electronic time step. These values are summed over the course of the nuclear step to give the left Riemann sum approximation to the integral in Eq. (1.11). Analytical expressions for the non-adiabatic couplings for states represented in the electronic structure framework of RPA or linear response TDDFT have been previously derived by numerous groups.[47–52] A slightly different derivation of the working equations used in this work to calculate first-order non-adiabatic coupling matrix elements between the ground and excited states resolved via random phase approximation (RPA, i.e. "linear response TDDFT/TDHF") based methods is given in Appendix 1.

Since the nuclei at all times evolve according to the forces associated with a single adiabatic state (and nuclear momenta are explicitly rescaled after hops to conserve total energy) energy conservation of exactly the same quality as the adiabatic, "Born-Oppenheimer" molecular dynamics (BOMD) is trivially guaranteed by the surface-hopping algorithm. Both the velocity Verlet and midpoint methods are second-order integration schemes. However, since the $\mathbf{d}_{jk}$, $\dot{\mathbf{R}}_0$, and $\mathbf{V}_{jj}$ are calculated only at intervals of Δt_n, these quantities are interpolated between t and $t + \Delta t_n$ to account for their linear changes during nuclear time steps in the electronic propagation (see Fig. 2.1 for schematic representation and pseudocode.) This interpolation complicates the error analysis of the resulting method somewhat, since it is a source of error in the electronic propagation that isn't a result of the inaccuracy of the numerical integration of Eq. (2.2), but of the assumed linearity of the interpolated quantities across the nuclear time step. The nuclear time step should therefore be chosen sufficiently small to not only conserve total energy of the system as in the BOMD scheme, but also to not under-sample regions of the nuclear phase space where $\mathbf{d}$ is non-linear in $\mathbf{R}$ over the distance $\dot{\mathbf{R}} \cdot \Delta t_N$.

When the nuclear evolution brings two adiabats into degeneracy, the derivative couplings ($\mathbf{D}$ and $\mathbf{d}$) between those states become unboundedly large in magnitude and the involved

PES's exhibit discontinuities. When these regions of strong coupling are extremely localized in the nuclear phase space, the finite time-step of the nuclear dynamics can cause the crossing points to be skipped over in some trajectories. This scanario becomes more common for larger systems of weakly-interacting fragments. In this case, it is common practice to utilize a basis of diabatic states, since off-diagonal matrix elements of the electronic Hamiltonian in the diabatic representation are well-defined even at PES crossings, and moreover these electronic couplings are generally well-behaved functions of the nuclear coordinates, $\mathbf{R}$.[80] Beyond transformation to a (locally quasi-)diabatic basis, approaches to identify PES crossings directly within the adiabatic basis based on the overlap of the electronic eigenfunctions at adjacent Δt_N can also be utilized to enforce transition at PES crossings externally to the FSSH algorithm.[81,82]

2.2 Meta-Surface-Hopping Dynamics

A longstanding criticism of TSH approaches has been the sheer quantity of trajectories that must be computed in order to ensure the convergence of results. If the dynamical process of interest occurs over long ($\sim ns$ and slower) time-scales, or is fast, but initiated by some rare event, TSH is of little practical utility. In this section, we introduce a "meta-surface-hopping dynamics" method (MSH) for expediting the estimation of non-adiabatic relaxation time constants. This approach, in the similar spirit as the "meta-dynamics"[83,84], combines time-dependent perturbation theory (TDPT) with the direct *ab initio* TSH to achieve an optimal balance of computational expense and accuracy. The central idea of the meta-dynamics approach is to bias the evolution of a system toward a desired low-probability pathway, and then mathematically relate results of the biased dynamics to those for the unbiased system.[83,84] In this way, rare events can be efficiently investigated directly in the time domain, and the effect of the biasing on the resulting dynamics can be accounted for *post facto.* While the MSH method is certainly not the first method to be put forth for expediting the description of slow non-adiabatic processes in TSH,[85–87] the current work (to the authors' best knowledge) represents the first such attempt to combine the benefits of direct dynamics and TDPT to this end.

The choice of rare event biasing depends on whether or not there exists a mathematical expression that can resolve the effect of the biasing on the dynamical observables. TDPT is a reliable method, with some degree of scrutiny, for describing the response of a system in the instants following the application of a small perturbation. Recall that the rate of transition from state i to j mediated by a time-independent external potential can be approximated by the 'Fermi's golden rule' (in atomic units) derived using TDPT[88–90]:

$$\Gamma_{ij} = 2\pi \left| \left\langle \Phi_i \middle| \dot{\Phi}_j \right\rangle \right|^2 \delta(E_i - E_j) \tag{2.7}$$

A quasi-static approximation may be used to cast Eq. (2.7) into a time-dependent expression:

$$\Gamma_{ij}(t) = 2\pi \left| \left\langle \Phi_i(t) \middle| \dot{\Phi}_j(t) \right\rangle \right|^2 \delta(E_i(t) - E_j(t)) \tag{2.8}$$

As the character of the initial and final states change with nuclear motion, so does the transition rate. By following the explicit time evolution of the adiabats with molecular dynamics, the electronic states to which the Fermi's golden rule rate expression is applied are sampled from an ensemble of thermally accessible nuclear configurations. The ensemble-averaged expression for the transition rate is then given by:

$$\langle \Gamma_{ij} \rangle = \frac{2\pi}{t'} \int_0^{t'} dt \left| \left\langle \Phi_i(t) \middle| \dot{\Phi}_j(t) \right\rangle \right|^2 \delta(E_i(t) - E_j(t)) \tag{2.9}$$

Using the chain rule, we can obtain the relationship between the non-adiabatic transition rate and the non-adiabatic coupling strength,

$$\begin{aligned} \langle \Gamma_{ij} \rangle &= \frac{2\pi}{t'} \int_0^{t'} dt \left| \dot{\mathbf{R}}_j(t) \cdot \langle \Phi_i | \nabla_{\mathbf{R}_j} | \Phi_j \rangle \right|^2 \delta(E_i - E_j) \\ &= \frac{2\pi}{t'} \int_0^{t'} dt \left| \dot{\mathbf{R}}_j(t) \cdot \mathbf{d}_{ij}(t) \right|^2 \delta(E_i - E_j) \end{aligned} \tag{2.10}$$

Equation (2.10) suggests that the time averaged non-adiabatic transition rate depends linearly on the nuclear kinetic energy ($\propto \dot{\mathbf{R}}^2$) and quadratically on the non-adiabatic coupling strength. Increasing the simulation temperature will increase the non-adiabatic transition rate. However, the nature of the dynamics will be severely modified as the nuclei are free to traverse different reaction pathways at substantially elevated temperatures. In contrast, there are two advantages of directly biasing the time-dependent non-adiabatic coupling in Eq. (2.10). First, it is a "cold" biasing technique in which the system temperature is not modified. Second, because of the quadratic dependence, one can quickly obtain meaningful result without applying a large biasing.

In this work, we simply use and test a uniform biasing approach,

$$\mathbf{d}^{\text{biased}}(t) = \kappa\,\mathbf{d}(t) \tag{2.11}$$

where κ is a time-independent biasing factor for all states and at all nuclear configurations. With such a biased time-dependent non-adiabatic coupling, it is rather easy to show from Eq. (2.10) that

$$\left\langle \Gamma^{\text{biased}} \right\rangle \approx \kappa^2 \left\langle \Gamma^{\text{unbiased}} \right\rangle . \tag{2.12}$$

With Eq. (2.12), the effect of biased time-dependent non-adiabatic coupling can be accounted for retroactively via first-order TDPT (i.e. Fermi's golden rule). Once well-converged results for the biased dynamics have been collected, one can relate the dynamics of the biased system back to those of the unbiased system via TDPT.

It is obvious that the dynamics are unaffected by the biasing in the limit of zero coupling, and the correct asymptotic behavior is ensured. Nonetheless, one must ensure that κ is not so large that regions of the nuclear phase space that would be extensively sampled during the unbiased dynamics go unexplored as a result of over-promoted state switches. The stochastic nature of the surface-hopping algorithm builds in some insurance against this behavior, but in the event that excessive bias is applied, the dynamical processes that were rare in the unbiased dynamics dominate in the biased dynamics, and *vice versa.* Numerous trajectories would then be required to explore the regions of phase space that were frequently sampled in the unbiased dynamics, negating the practical advantage of applying the bias in the first place. Therefore, a balance must be struck in which the scaling factor is sufficiently large to promote the rare event, but not so large as to preclude electronically adiabatic evolution in coupled regions of the adiabatic PES.

In general, one should seek to use the smallest κ that produces non-adiabatic transitions at a rate that permits their study. The reaction coordinate for the non-adiabatic process can be characterized, and an appropriate range of scaling factors can be deduced from sample trajectories by analyzing the extent of sampling of the nuclear phase space prior to the non-adiabatic transition. Note, that situations may arise in which the magnitudes of κ needed to enable non-adiabatic processes to occur at a tractable rate do not uphold the 'linear-response' regime in which the first-order TDPT is reliable. Not all un-biased observables are straightforwardly recoverable from the biased dynamics either. If a reliable relationship between the property of interest and the strength of the perturbation can be established (as is done here for the non-radiative transition rates by application of the Fermi's golden rule) the un-biased property can in principle be recovered from sufficiently many biased trajectories. However, the nuclear dynamics following a premature/late state switch relative to the unbiased dynamics can be substantially altered by the excess/deficit of energy transferred into nuclear momentum along the coupling vector when a hop occurs early/late relative to the unbiased rate. Observables that depend on a faithful reproduction of the nuclear dynamics following the non-adiabatic transition may therefore suffer substantial statistical degradation. Also, even when the form of the fitted function is well motived, extrapolation of a fitted function far from the region of fitted data can be a dubious practice (especially if there is non-trivial error in the fit.) Furthermore, we have only considered one-dimensional problems in this work, and it is not obvious that the internal consistency between the perturbation theory and surface hopping rates should be reasonably maintained when moving to higher dimensional problems. These caveats should be considered prior to application of the approaches outlined here.

2.3 Application to Photoisomerization of Protonated Formaldimine

In this work, we will demonstrate that non-adiabatic transition rates from the direct MSH dynamics are consistent with Eq. (2.12) derived from the TDPT expression. Details of a study validating the MSH approach on a single avoided crossing model problem are found in Appendix 2. As a practical test of the implementation outlined in the methodology section, we performed a set of direct TSH trajectories to track the non-radiative decay of the first excited (singlet) state of protonated formaldimine, $H_2C{=}NH_2^+$. We simulate a Boltzmann ensemble of formaldimine molecules at room temperature (298K). For a specific vibrational mode with a given Boltzmann sampled vibrational energy, the initial phase (nuclear positions and momenta) was chosen randomly and classically within the harmonic oscillator approximation.[91,92] The total angular momentum was set to zero. Since the real potential energy surface is not strictly harmonic, the initial vibrational coordinates and momenta generated by this procedure were scaled to correct for the anharmonicity. This ensemble assumes a broad geometric distribution of vibrational phases of the initial ground state from which the vertical excitation to the first singlet excited state takes place. A total of 40 initial conditions were prepared for dynamic studies. The electronic wave function was initialized as a pure state comprised exclusively of the first excited (singlet) state of the molecule, in order to emulate a Franck-Condon type vertical photo-excitation of the molecule at time zero of the simulation. 5 sets of trajectories from the 40 initial conditions were integrated for 1 ps, each employing a different biasing factor, κ, listed in Tab. 2.1. To enable direct comparison of results across the different sets of trajectories, identical initial conditions and random number generator seeds were used for the 5 different swarms. The values of Δt_n and Δt_e used in all simulations were 0.1 fs and 0.004 fs respectively. These step sizes ensured energy conservation to within 0.03 kcal throughout the picosecond trajectories. In the following simulations, electronic degrees of freedom are modeled at the TDA-RPA-HF/6-31g(d,p) level of theory. Since the lower-scaling Tamm-Dancoff approximation (TDA) to the RPA yields nearly equivalent non-adiabatic couplings and excitation energies for the current system, TDA-RPA was used to resolve the excited state electronic structure in this case study.

κ	τ_e	τ_g	B	τ	σ^2
125	745	2813	0.408	1970	0.055
250	3089	826	0.159	1185	0.033
500	673	717	0.841	680	0.028
1000	395	144	0.387	241	0.021
1500	N/A	114	0.0	114	0.022

Table 2.1: Parameters for the non-radiative decay profile of the S_1 state of $H_2C{=}NH_2^+$ fit to a function of the form: $f(t) = Be^{-t/\tau_e} + (1-B)e^{-\frac{t^2}{2\tau_g^2}}$. σ^2 are the variances in the residuals for the fitted decay functions, calculated by $\sigma^2 = \frac{1}{N-1}\sum_{i=1}^{N}(f(t_N)_{\text{fit}} - f(t_N))^2$. τ are reported in units of Δt_N, or $s \times 10^{-16}$.

Figure 2.2 shows the potential energy surfaces of the ground S_0 and the first excited state S_1, and the analytical non-adiabatic coupling strength as a function of C=N bond rotation of the $H_2C{=}NH_2^+$ molecule. As expected, the energy gap between S_0 and S_1 states is the smallest when the C=N bond is rotated by 90 ° from the ground state equilibrium geometry, where the non-adiabatic coupling strength also reaches its maximum. However, the smallest gap is still $\sim$ 1.8 eV and the non-adiabatic coupling strength is only $\sim 3\times$ larger than at the ground state equilibrium structure. This cursory analysis suggests that non-adiabatic transitions along this coordinate are rare events — an ideal test case to showcase the MSH dynamics.

As a benchmark for the effects of the biasing strategy on the PES sampling, we have plotted the density of nuclear position eigenstates (see Fig. 2.3) sampled prior to relaxation from S_1. At the largest κ employed in this work, under-sampling of regions of the phase space occurs as a result of over-promotion of non-adiabatic transitions. The $\kappa = 1500$ dynamics would, in general, be discarded on these grounds, but the symmetry of the nuclear phase space for the particular system under investigation here makes the effect of the induced non-ergodicity less pronounced.

The decay profiles were fitted to Gaussian plus exponential functions (see Fig. 2.4). Since only two states are involved in the relaxation, multi-exponential character isn't expected in the decay profile. However, Gaussian shaped relaxation profiles are included in the fitting function in order to quantify the non-Markovian, phonon memory-dependent contributions to the relaxation dynamics.[93] The resulting fit parameters and time constants for the decay are presented in Tab. 2.1 along with the explicit form of the fitting function, and plotted in Fig. 2.5 along with the trendline of the form anticipated by the TDPT.

The resulting relaxation rates agree with the quadratic scaling predicted via the TDPT. Some of the deviation from the expected scaling can be attributed to the limited number of trajectories included in this investigation. Better agreement is seen for larger κ where a greater portion of trajectories undergo hops. So, even though the same initial conditions were used for each swarm, the resulting rates are better statistically converged for the larger κ cases ((see variances of the residuals for each fitted function in Tab. 2.1) — another unique advantage for the MSH method. Once the required statistical convergence has been achieved for the relaxation rate at a few different biasing strengths, the decay constants can be fitted to a function that is quadratic in κ. The prefactor of the fitted quadratic function (see Fig. 2.5), $3.96{\times}10^7 s^{-1}$ for the current study, gives the MSH extrapolatory estimate for the relaxation rate for the unbiased system, i.e. for $\kappa = 1$. The results indicate that the studied process is indeed expected to be quite slow with respect to the time-step of the dynamics.

Conclusions and Perspective

A direct *ab initio* (meta-)surface-hopping dynamics approach was presented, where energies, analytical forces and non-adiabatic couplings are computed "on-the-fly". A split integrator was implemented to facilitate the computation without compromising energy conservation. Analytical derivative coupling within the random phase approximation framework was derived and the working equations efficiently implemented. We also presented a time-dependent perturbation theory (TDPT) based meta-dynamics approach to bias the dynamics toward non-adiabatic rare events. This approach aims to accelerate the acquisition of temporal properties of systems exhibiting electronic non-adiabaticity in a systematic, reproducible fashion.

As a test of the non-adiabatic meta-surface-hopping method, we calculated several sets of 40 trajectories with different biasing strengths for photo-isomerizing protonated formaldimine. We have shown that the trend predicted via the TDPT expression holds when comparing the dynamics of swarms with different biasing factors, suggesting the internal consistency of our meta-dynamics/TDPT approach.

Appendix 1: First-Order Non-Adiabatic Coupling Matrix Elements between Ground and Excited States

The mathematical expressions for derivative coupling within the random phase approximation (RPA) or the linear response TDDFT framework have have been previously presented by other groups.[47–52] Here we present slightly different derivations for obtaining an efficient working expressions implemented in this work for the ground to excited state derivative coupling. In the present work we adopt the notation that indices i, j, k, l refer to occupied molecular orbitals (MO), a, b, c, d refer to virtual MOs and p, q, r, s refer to general MOs. $\mu, \nu, \lambda, \delta$ will be used to label atomic orbital (AO), and σ, σ' to label different spin orientations.

We cast the derivative coupling into second quantized form as a scattering problem off of a single body, anti-Hermitian operator, ∇_ξ,

$$\nabla_\xi = \sum_{pq\sigma} \langle p;\sigma \left|\nabla_\xi\right| q;\sigma\rangle \, a^\dagger_{p\sigma} a_{q\sigma} \tag{A1.1}$$

where $a^\dagger_p$ and a_q are the second-quantized fermionic creation and annihilation operators respectively.

Recalling the expression for the non-adiabatic coupling (derivative coupling) with respect to nuclear coordinate ξ between ground and I-th excited state, d^ξ_{0I}, we may recast it into a general second quantized expression,

$$d_{0I}^{\xi} = \langle \Psi_0 \left| \nabla_\xi \right| \Psi_I \rangle = \sum_{pq\sigma} \left\langle \Psi_0 \left| a_{p\sigma}^{\dagger} a_{q\sigma} \right| \Psi_I \right\rangle \langle p;\sigma \left| \nabla_\xi \right| q;\sigma \rangle \quad . \tag{A1.2}$$

In the case where the ground state is expressed as a single Slater determinant of Hartree-Fock (HF) or Kohn-Sham (KS) orbitals, the I-th excited state can be written as a non-Hermitian excitation operator $\hat{T}^I$ acting on the ground (reference) state

$$\left| \Psi^I \right\rangle = \hat{T}^I \left| \Psi_0 \right\rangle = \sum_{rs\sigma} t_{rs\sigma}^{I} a_{r\sigma}^{\dagger} a_{s\sigma} \left| \Psi_0 \right\rangle \quad . \tag{A1.3}$$

For RPA and the Tamm-Dancoff approximation (TDA) thereof, the expression for $\mathbf{T}$ takes the convenient forms

$$\mathbf{T}_{TDA}^{I} = \begin{pmatrix} \mathbf{0} & \mathbf{0} \\ \mathbf{X}_I & \mathbf{0} \end{pmatrix} \qquad \mathbf{T}_{RPA}^{I} = \begin{pmatrix} \mathbf{0} & \mathbf{Y}_I^{\dagger} \\ \mathbf{X}_I & \mathbf{0} \end{pmatrix} \tag{A1.4}$$

where $\left| \mathbf{X}^I \right\rangle$ and $\left| \mathbf{X}^I, \mathbf{Y}^I \right\rangle$ are the transition vectors for the I-th excited state for TDA and RPA respectively. Using the expression for the I-th excited state from Eq. (A1.3), Eq. (A1.2) may be evaluated as

$$d_{0I}^{\xi}(\text{TDA}) = -\sum_{ia\sigma} X_{ia\sigma}^{I} \langle i;\sigma \left| \nabla_\xi \right| a;\sigma \rangle \tag{A1.5}$$

$$d_{0I}^{\xi}(\text{RPA}) = -\sum_{ia\sigma} \left(X_{ia\sigma}^{I} - Y_{ia\sigma}^{I} \right) \langle i;\sigma \left| \nabla_\xi \right| a;\sigma \rangle \tag{A1.6}$$

Working expressions for the derivative operator in the basis of single particle molecular orbitals may be trivially obtained via direct differentiation.

$$\begin{aligned}\langle p;\sigma\left|\nabla_\xi\right|q;\sigma\rangle &= U^{\xi}_{pq\sigma} + S^{([\xi])}_{pq\sigma} \\ S^{([\xi])}_{pq\sigma} &= \sum_{\mu\nu} C^{*}_{\mu p\sigma}\left\langle \mu \mid \nu^{\xi}\right\rangle C_{\nu q\sigma}\end{aligned} \tag{A1.7}$$

where $\mathbf{U}^{\xi}$ is the solution to the coupled-perturbed Kohn-Sham/Hartree-Fock (CPKS/CPHF) equations

$$\begin{aligned}&\sum_{jb\sigma'}(\mathbf{A}+\mathbf{B})_{ia\sigma,jb\sigma'}U^{\xi}_{jb\sigma'} = -R_{ia\sigma} \\ &R_{ia\sigma} = h^{(\xi)}_{ia\sigma} + v^{H(\xi)}_{ia\sigma} + v^{XC(\xi)}_{ia\sigma} - \epsilon_i S^{(\xi)}_{ia\sigma} - \frac{1}{2}G^{+}_{ia\sigma}\left[S^{(\xi)}_{oo}\right]\end{aligned} \tag{A1.8}$$

where the parenthetical superscript denotes differentiation at fixed MO's, $\mathbf{h}$ is the single particle core hamiltonian, $\{\epsilon_i\}$ are the occupied orbital eigenenergies, $\mathbf{S}^{\xi}$ is the total derivative of the AO overlap matrix in the MO basis, v^{H} is the static Hartree term, and v^{XC} is the static KS-XC potential, which is related to the exchange-correlation kernel, E_{XC}, by

$$v^{\mathrm{XC}}_{ia\sigma} = \sum_{\mu\nu} C^{*}_{\mu i}\left\langle \mu \left| \frac{\partial E_{XC}}{\partial \rho_\sigma} \right| \nu \right\rangle C_{\nu a} \tag{A1.9}$$

$\mathbf{G}^{+}$ is the electron-repulsion-integral tensor contracted with the occupied-occupied block of the total derivative of the overlap in the MO basis, $\mathbf{S}^{\xi}_{oo}$

$$G^{+}_{ia\sigma}\left[S^{(\xi)}_{oo}\right] = \sum_{jk\sigma'}\Big(2(ia\sigma|jk\sigma') - C_x\delta_{\sigma\sigma'}\left[(ik\sigma|ja\sigma)+(ij\sigma|ak\sigma)\right] + 2(ia\sigma|f^{\sigma\sigma'}_{xc}|jk\sigma')\Big)\, S^{(\xi)}_{jk} \tag{A1.10}$$

where $C_x \in [0,1]$ is the scaling factor for exact HF exchange in hybrid DFT and $f^{\sigma\sigma'}_{XC}$ is related to the XC kernel by

$$f^{\sigma\sigma'}_{XC} = \frac{\delta^2 E_{XC}\left[\rho(\mathbf{r},\mathbf{r}')\right]}{\delta\rho_\sigma(\mathbf{r})\delta\rho_{\sigma'}(\mathbf{r}')} \tag{A1.11}$$

Inserting Eq. (A1.7) into Eq. (A1.5) and Eq. (A1.6) yields a simple yet inefficient working expressions for the derivative coupling

$$d_{0I}^{\xi}(\text{TDA}) = -\sum_{ia\sigma} X_{ia\sigma}^{I} U_{ia\sigma}^{\xi} - \sum_{ia\sigma} X_{ia\sigma}^{I} S_{ia\sigma}^{([\xi])} \tag{A1.12}$$

$$d_{0I}^{\xi}(\text{RPA}) = -\sum_{ia\sigma} \left(X_{ia\sigma}^{I} - Y_{ia\sigma}^{I}\right) U_{ia\sigma}^{\xi} - \sum_{ia\sigma} \left(X_{ia\sigma}^{I} - Y_{ia\sigma}^{I}\right) S_{ia\sigma}^{([\xi])} \tag{A1.13}$$

One can eliminate the explicit dependence on $\mathbf{U}^{\xi}$ via a transformation akin to the Sternheimer-Dalgarno interchange theorem[94,95]

$$d_{0I}^{\xi}(\text{TDA}) = \sum_{ia\sigma} \tilde{Z}_{ia\sigma}^{\text{TDA},I} R_{ia\sigma}^{\xi} - \sum_{ia\sigma} X_{ia\sigma}^{I} S_{ia\sigma}^{([\xi])} \tag{A1.14}$$

$$d_{0I}^{\xi}(\text{RPA}) = \sum_{ia\sigma} \tilde{Z}_{ia\sigma}^{\text{RPA},I} R_{ia\sigma}^{\xi} - \sum_{ia\sigma} \left(X_{ia\sigma}^{I} - Y_{ia\sigma}^{I}\right) S_{ia\sigma}^{([\xi])} \tag{A1.15}$$

$$\sum_{jb\sigma'} (\mathbf{A}+\mathbf{B})_{ia\sigma,jb\sigma'} \tilde{Z}_{jb\sigma'}^{\text{TDA},I} = X_{ia\sigma}^{I} \tag{A1.16}$$

$$\sum_{jb\sigma'} (\mathbf{A}+\mathbf{B})_{ia\sigma,jb\sigma'} \tilde{Z}_{jb\sigma'}^{\text{RPA},I} = X_{ia\sigma}^{I} - Y_{ia\sigma}^{I} \tag{A1.17}$$

While the solution of Eq. (A1.16) cannot be avoided, the solution of Eq. (A1.17), as was first recognized by Furche,[50] is known *a priori*,

$$\tilde{Z}_{ia\sigma}^{\text{RPA},I} = \frac{1}{\omega_I}(X_{ia\sigma}^{I} + Y_{ia\sigma}^{I}) \tag{A1.18}$$

where ω_I is the excitation energy corresponding to the transition vector $\left|\mathbf{X}^{I}, \mathbf{Y}^{I}\right\rangle$. Transforming Eq. (A1.14) and Eq. (A1.15) into the AO basis, one can obtain an efficient working expression for the derivative coupling closely resembling that of the ground state gradient

$$\begin{aligned} d_{0I}^{\xi}(\text{TDA/RPA}) = &\sum_{\mu\nu\sigma} h_{\mu\nu}^{\xi} \tilde{Z}_{\mu\nu\sigma}^{\text{TDA/RPA},I} + \sum_{\mu\nu\sigma} v_{\mu\nu}^{XC(\xi)} \tilde{Z}_{\mu\nu\sigma}^{\text{TDA/RPA},I} + \sum_{\mu\nu\sigma} S_{\mu\nu}^{\xi} \tilde{W}_{\mu\nu\sigma}^{\text{TDA/RPA},I} \\ &+ \sum_{\mu\nu\lambda\delta\sigma\sigma'} (\mu\nu|\lambda\delta)^{\xi}\, \tilde{\Gamma}_{\mu\nu\sigma,\lambda\delta\sigma'}^{\text{TDA/RPA},I} + \sum_{\mu\nu\sigma} \tilde{T}_{\mu\nu\sigma}^{\text{TDA/RPA},I} S_{\mu\nu}^{[\xi]} \end{aligned} \tag{A1.19}$$

where

$$\tilde{T}_{\mu\nu\sigma}^{\text{TDA},I} = \sum_{\mu\nu} C_{\mu i}^{*} X_{ia\sigma}^{I} C_{\nu a}; \qquad \tilde{T}_{\mu\nu\sigma}^{\text{RPA},I} = \sum_{\mu\nu} C_{\mu i}^{*} \left(X_{ia\sigma}^{I} - Y_{ia\sigma}^{I} \right) C_{\nu a}$$

$$\tilde{W}_{ia\sigma}^{\text{TDA/RPA},I} = \epsilon_{i\sigma} \tilde{Z}_{ia\sigma}^{\text{TDA/RPA},I}; \quad \tilde{W}_{ij\sigma}^{\text{TDA/RPA},I} = \frac{1}{1+\delta_{ij}} G_{ij\sigma}^{+} \left[\tilde{Z}_{ia\sigma}^{\text{TDA/RPA},I} \right]; \quad \tilde{W}_{ab\sigma}^{\text{TDA/RPA},I} = 0$$

$$\tilde{\Gamma}_{\mu\nu\sigma,\lambda\delta\sigma'}^{\text{TDA/RPA},I} = \frac{1}{2} \left(2 \tilde{Z}_{\mu\nu\sigma}^{\text{TDA/RPA},I} D_{\lambda\delta\sigma'} - C_x \delta_{\sigma\sigma'} \left[\tilde{Z}_{\mu\delta\sigma}^{\text{TDA/RPA},I} D_{\lambda\nu\sigma} + \tilde{Z}_{\nu\delta\sigma}^{\text{TDA/RPA},I} D_{\lambda\mu\sigma} \right] \right)$$

where $\mathbf{D}$ is the ground state KS/HF density.

Appendix 2: Meta-Surface-Hopping Method Validated on 1-Dimensional Single Avoided Crossing Problem

The robustness of the MSH method relies on the surface hopping and perturbative-derived transition rates being affected proportionately by an artificial magnification of the coupling strength between states. As was derived in the main text (Eq. (2.12)), the Fermi's golden rule transition probability depends quadratically on the biasing strength parameter, κ. However, the coupling strength only explicitly enters into the FSSH transition probability expression (Eq. (1.11)) linearly. For these two approaches to yield consistent behavior upon scaling of the coupling, the effect of the heightened coupling on the composition of the evolving electronic wavepacket must account for the "missing power" of the scaling factor in the FSSH transition probability expression. From Eq. (3.3), it is clear that the evolution of the density matrix elements that enter into the FSSH probability expression depends nonlinearly on the scaling factor, κ, so unlike the TDPT approach, no simple closed-form relationship can be derived between κ and the FSSH transition probability. Instead, numerical evidence that the inclusion of the magnified coupling in the electronic propagation effectively accounts for the apparent discrepancy between the surface hopping and TDPT transition probabilities must suffice.

To numerically probe the relationship between the FSSH relaxation rates and a constant factor scaling the coupling strength between the quantum states of a system, the MSH method was applied to a single avoided crossing model problem defined by the following Hamiltonian in the diabatic representation[61]:

$$\begin{aligned}
V_{11}(R) &= A\left[1-\mathrm{Exp}\left[-BR\right]\right],\ R \geq 0,\\
V_{11}(R) &= -A\left[1-\mathrm{Exp}\left[-BR\right]\right],\ R \leq 0,\\
V_{22}(R) &= -V_{11}(R),\\
V_{12}(R) &= V_{21}(R) = C\,\mathrm{Exp}\left[-DR^2\right].
\end{aligned} \tag{A2.1}$$

Surface hopping trajectories were evaluated directly in the diabatic basis. For the MSH biasing procedure, the diabatic couplings (rather than the analogous derivative couplings between adiabats which vanish in the diabatic representation) were uniformly scaled by κ. For the purposes of isolating the effect of the scaled couplings on the surface hopping rates, only relaxation events prior to the diabatic surface crossing (i.e. those induced by surface hops) are considered in the transition rate statistics. In this way, a finite maximum lifetime was effectively imposed on the excited state, leading to a non-zero rate for the $\kappa \to 0$ limit that was accounted for prior to the collection of transition statistics.

10,000 independent trajectories were computed for different values of κ to determine the mean (surface hopping) lifetimes for each biasing strength. All trajectories were initialized in the upper diabatic state, and share common classical initial conditions and model parameters ($R(0) = -2, \dot{R}(0) = 0, A = 0.01, B = 1.6, C = 0.005$, and $D = 1.0$.) The quadratic dependence of the FSSH transition rate on the biasing strength (see Fig. 2.6) observed for the model problem shows with a high degree of statistical certainty that average hopping probabilities are consistent with the TDPT result for certain ranges of biasing strengths, and that hybrid dynamical/perturbative methods are a promising direction for investigating slow transitions via biased time-domain simulations.

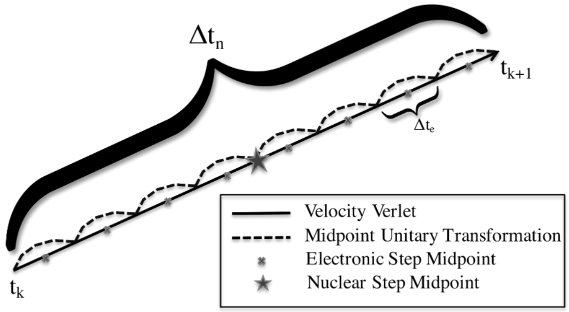

```
for $1 \leq k \leq maxstep$ do
    Get $\mathbf{V}(t_k)$ for all states
    Get $\mathbf{d}(t_k)$ between all states
    Get $\nabla_{R_0}\mathbf{V}(t_k)$ for current state
    if (not first step since start/hop) then
        Propagate $\dot{\mathbf{R}}_\mathbf{0}(t_{k-1/2}) \rightarrow \dot{\mathbf{R}}_\mathbf{0}(t_k)$ (Eq. (11a))
        for $1 \leq j \leq (\Delta t_n/\Delta t_e)$ do
            Use $\mathbf{U}(t_{j+1/2})$ to Propagate $\mathbf{c}(t_j) \rightarrow \mathbf{c}(t_{j+1})$ (Eqs. (14) to (16))
            Calculate (and collect) integrand of Eq. (10) scaled by $\Delta t_e$
        end for
        Compare each $g$ to uniformly distributed random number $\eta \in \mathcal{U}\{0,1\}$
        if $g > \eta$ then
            Calculate kinetic energy component along coupling vector, $T_d$
            if $T_d > \Delta\mathbf{V}$ then
                Switch current state
                Scale $\dot{\mathbf{R}}_\mathbf{0}$ to conserve total energy
            end if
        else
            Calculate $\mathbf{R}_\mathbf{0}(t_{k+1})$ and $\dot{\mathbf{R}}_\mathbf{0}(t_{k+1/2})$ (Eqs. (11b) to (11c))
        end if
    end if
end for
```

Figure 2.1: Schematic representation of the split time-scale integration scheme used in the current implementation.

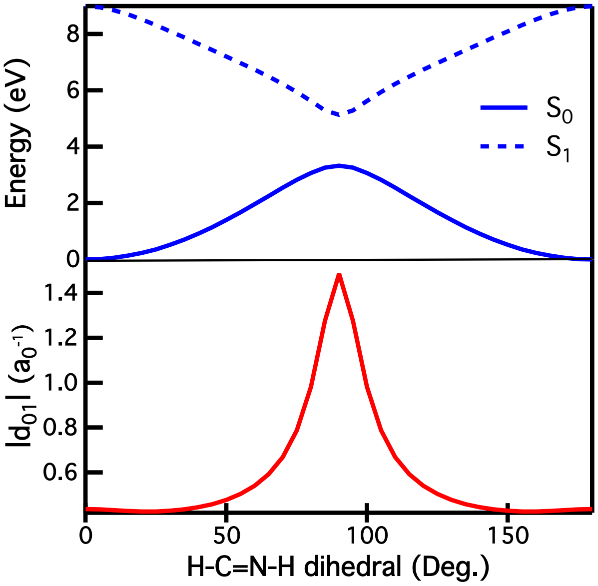

Figure 2.2: S_0 and S_1 PES's (top panel) and corresponding derivative coupling magnitude (bottom panel) as a function of H-C=N-H dihedral. All other internal coordinates are fixed at their equilibrium geometry values. Reproduced with permission from reference 1

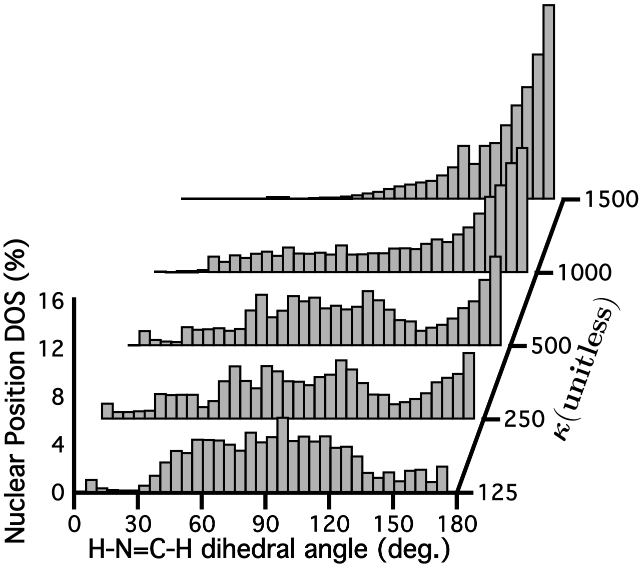

Figure 2.3: Histograms showing the density of nuclear position states sampled prior to relaxation to the ground state as a function of the biasing factor, κ. So as not to distinguish between the degenerate clockwise and counter-clockwise rotation pathways about the double-bond in this analysis, identical configurations with respect to this symmetry have been binned together. Dihedrals are computed between the two hydrogens "*trans*" to one another in the initial condition, so that the "*cis*" and "*trans*" isomers are well-defined and spurious non-ergodic behavior in the DOS induced by large κ can be resolved. Reproduced with permission from reference 1

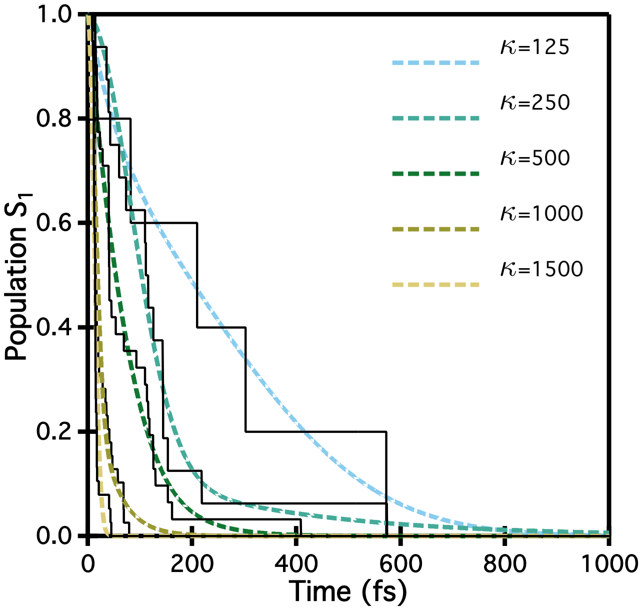

Figure 2.4: Examples of a vibrationally-induced relaxation profile from S_1 state for $H_2C{=}NH_2^+$ resulting from the MSH dynamics with κ =125, 250, 500, 100, and 1500 (black traces) and corresponding exponential plus Gaussian fitted functions (colored, dashed traces.) Reproduced with permission from reference 1

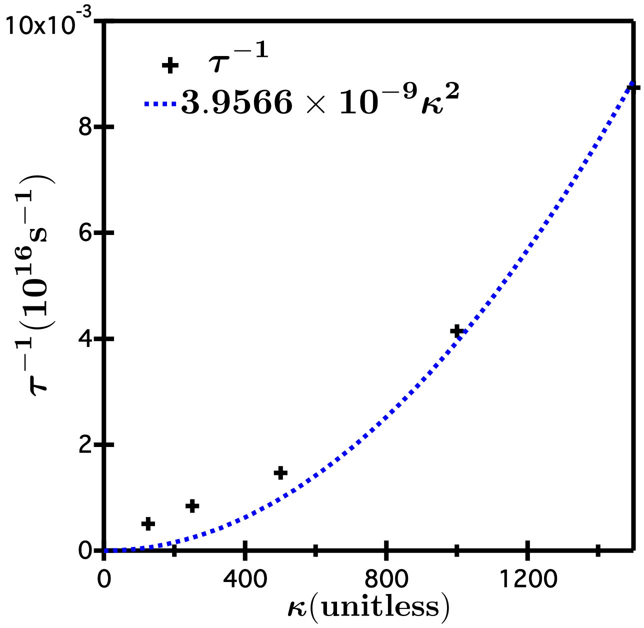

Figure 2.5: Plot of relaxation rates from Tab. 2.1 showing the trend for the relaxation rate (τ^{-1}, black markers) as a function of the biasing factor, along with a least-squares fit of the rates as a function of biasing factor that is consistent with Fermi's golden rule (i.e. $\tau^{-1} \propto \kappa^2$). Reproduced with permission from reference 1.

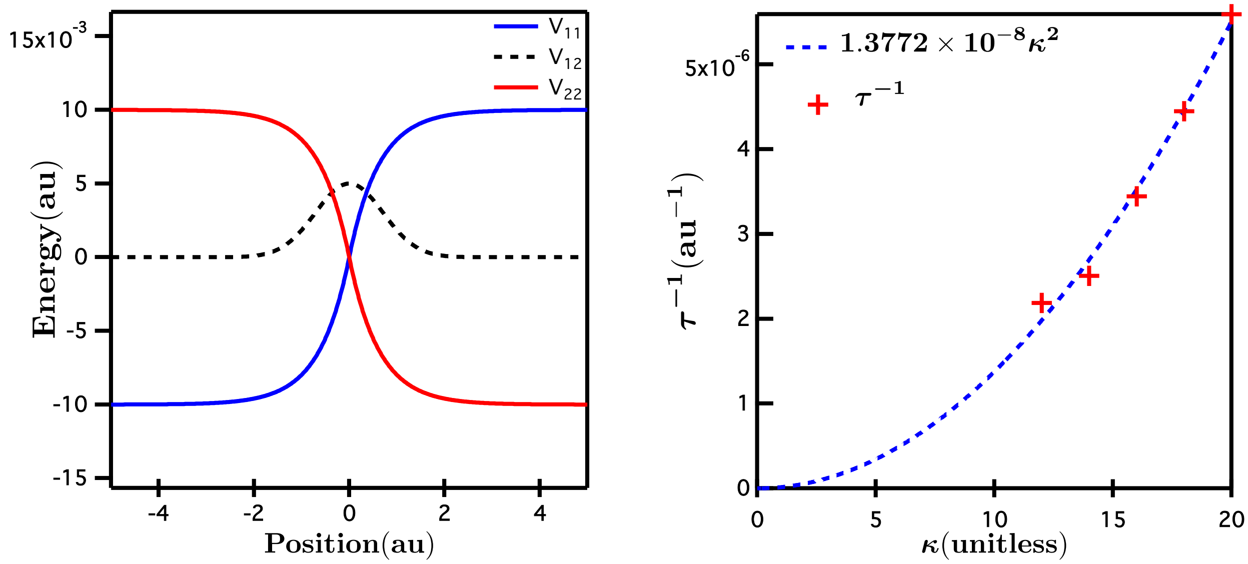

Figure 2.6: Left: Diabatic energy curves and couplings in the region of the surface crossing for the single avoided crossing model problem. Right: Quadratic fit to the surface-hopping transition rates as a function of a coupling biasing factor, κ, showing consistent proportionality with that expected from the Fermi's golden rule expression. Reproduced with permission from reference 1.

Chapter 3

MEAN-FIELD (“EHRENFEST”) DYNAMICS

3.1 Ehrenfest Dynamics Overview

In addition to the method provided in Chapter 1, the Ehrenfest method's working equations can also be derived by positing, from the onset, a single product ansatz for the full molecular wave function:

$$\Psi(\mathbf{r}, \mathbf{R}, t) = \Phi_{ele}(\mathbf{r}, t) \cdot \Omega_{nuc}(\mathbf{R}, t) \tag{3.1}$$

where $\mathbf{R}$ and $\mathbf{r}$ denote the nuclear and electronic coordinates.[18] Substituting a molecular wave function of the form in Eq. (3.1) into the time-dependent Schrödinger equation, multiplying on the left by Ω^*_{nuc} (or Φ^*_{ele}), and integration over all $\mathbf{R}$ (or $\mathbf{r}$) gives the time dependent self consistent field equations (i.e. the coupled equations of motion for the electronic degrees of freedom evolving in the mean-field nuclear potential and *vice versa*). Taking the classical limit for Ω gives an equation of motion for an electronic superposition state evolving along a nuclear trajectory, where the nuclei evolve classically according to the expectation value of the electronic potential (see Chapter 1 for full details of derivation starting from multi-configurational molecular wave function ansatz.) Further restricting Ω to be classical, and stationary (i.e. fixing the nuclear positions) gives the "real-time" time dependent self consistent field methods (RT-TDSCF), such as the RT-TD Hartree Fock (RT-TDHF) and the RT-TD density functional theory (RT-TDDFT) methods pioneered by Yabana and Bertsch[96], which have been gaining notoriety among electronic structure and computational spectroscopy communities due to their ability to capture full absorption spectra from a single electronic dynamics simulation.

3.2 Ehrenfest Dynamics in the Electronic Energy Eigenstate Basis

Here, we describe the implementation of the Ehrenfest mean-field mixed quantum/classical dynamics where the electronic superposition is expressed in a (truncated) basis of Born-Oppenheimer frame electronic energy eigenstates. That is, we express the electronic part of the wavefunction from Eq. (3.1), $\Phi_{ele}(\mathbf{R}, t)$, by:

$$\Phi_{ele}(\mathbf{r},t) = \sum_i c_i(t)\phi_i(\mathbf{r}) \tag{3.2}$$

where $\{\phi_i(t)\}$ are the electronic eigenfunctions from some electronic structure theory capable of resolving excited electronic states. The equation of motion for the electronic wavepacket in this basis is given by:

$$\begin{aligned} i\dot{c}_k(t) &= \sum_j \underbrace{\left(\delta_{kj}\mathbf{V}_{jj} - i\dot{\mathbf{R}}(t)\cdot\mathbf{d}_{kj}\right)}_{\mathbf{H}_{kj}} c_j(t) \\ &= \sum_j \mathbf{H}_{kj}c_j(t), \end{aligned} \tag{3.3}$$

where $\mathbf{V}_{kj} = \langle\phi_k|\mathscr{H}_r|\phi_j\rangle$, $\mathscr{H}_r$ is the full molecular Hamiltonian less the nuclear kinetic energy contribution, and $\mathbf{d}_{jk}$ is the first order non-adiabatic coupling vector between state k and j, i.e. $\mathbf{d}_{jk} = \langle\phi_j|\nabla_{\mathbf{R}}|\phi_k\rangle$.[97] Since we have choosen to work in the adiabatic basis, $\{\phi_j\}$ are eigenfunctions of the electronic Hamiltonian and $\mathbf{V}$ becomes diagonal. The time-dependence for the nuclear positions is given by the Newtonian equation of motion:

$$-\langle\nabla_R\mathbf{V}\rangle = \mathbf{m}\ddot{\mathbf{R}}_\mathbf{j} \tag{3.4}$$

where the brackets in Eq. (3.4) denote the expectation value. Eq. (3.3) is integrated via a norm-preserving unitary transformation:

$$\mathbf{c}(t+\Delta t_e) = \mathbf{U}\left(t+\frac{1}{2}\Delta t_e\right)\mathbf{c}(t) \tag{3.5}$$

$$\mathbf{U}(t) = \exp[-i\mathbf{H}(t)\Delta t_e] \tag{3.6}$$

where Δt_e is the electronic time step. The matrix exponentiation is carried out by first expressing $\mathbf{H}(t)$ in its eigenbasis:

$$\mathbf{H}(t) = \mathbf{\Lambda}(t)\,\epsilon(t)\,\mathbf{\Lambda}^\dagger(t) \tag{3.7}$$

Then the propagator can be easily constructed:

$$\mathbf{U}(t) = \mathbf{\Lambda}(t)\exp[-i\,\Delta t_e\,\epsilon(t)]\,\mathbf{\Lambda}^\dagger(t). \tag{3.8}$$

Eq. (3.4) is integrated via the velocity Verlet algorithm:

$$\dot{\mathbf{R}}_\mathbf{0}(t + \tfrac{1}{2}\Delta t_n) = \dot{\mathbf{R}}_\mathbf{0}(t) + \frac{1}{2}\ddot{\mathbf{R}}_\mathbf{0}(t)\Delta t_n \tag{3.9a}$$

$$\mathbf{R}_\mathbf{0}(t + \Delta t_n) = \mathbf{R}_\mathbf{0}(t) + \dot{\mathbf{R}}_\mathbf{0}(t + \tfrac{1}{2}\Delta t_n) \tag{3.9b}$$

$$\dot{\mathbf{R}}_\mathbf{0}(t + \Delta t_n) = \dot{\mathbf{R}}_\mathbf{0}(t + \tfrac{1}{2}\Delta t_n) + \frac{1}{2}\ddot{\mathbf{R}}_\mathbf{0}(t + \Delta t_n)\Delta t_n \tag{3.9c}$$

with nuclear time step Δt_n. For the current work, the same time step was chosen for the electronic and nuclear evolutions for consistency. The time-dependent dipole moment expectation value was evaluated by:

$$\mu(t) = \mathbf{Tr}[\mathbf{P}(t)\cdot\mathbf{d}]. \tag{3.10}$$

with the density matrix, $\mathbf{P} = \mathbf{c}^\dagger\mathbf{c}$ and the matrix elements of the dipole operator,$\mathbf{d}$, evaluated by:

$$d_{jk} = \langle\phi_j|\hat{\mu}|\phi_k\rangle \tag{3.11}$$

3.3 Ehrenfest Dynamics via Propagation of the Reduced Density Matrix

Here, we introduce the more generally applicable version of the Ehrenfest method, where we directly integrate the TDHF equations for the initial electronic state in the single-particle (orbital) basis. Note that this implementation doesn't require any knowledge of electronic energy eigenstates. This method has been previously implemented in the development version of the Gaussian suite of programs.[79,98]

The time-dependent Hartree-Fock/Kohn-Sham equations can be expressed as:

$$i\frac{\mathrm{d}\mathbf{P}(t)}{\mathrm{d}t} = [\,\mathbf{F}(t), \mathbf{P}(t)] \tag{3.12}$$

where $\mathbf{P}$ and $\mathbf{F}$ are the 1-electron reduced density matrix and Fock/Kohn-Sham matrices in an orthonormal basis. The modified midpoint and unitary transform (MMUT) algorithm is used to propagate the density in time[78]

$$\mathbf{P}(t_{n+1}) = \mathbf{U}(t_n) \cdot \mathbf{P}(t_{n-1}) \cdot \mathbf{U}^{\dagger}(t_n). \tag{3.13}$$

The unitary time evolution operator $\mathbf{U}(t_n)$ is constructed from the eigenvectors and eigenvalues of the Fock matrix

$$\begin{aligned} \mathbf{U}(t_n) &= \exp\left[-2i\,\Delta t\,\mathbf{K}(t_n)\right] \\ &= \mathbf{C}(t_n) \cdot \exp\left[-2i\,\Delta t\,\boldsymbol{\epsilon}(t_n)\right] \cdot \mathbf{C}^{\dagger}(t_n), \end{aligned} \tag{3.14}$$

The nuclear motion is purely classical, and is evaluated by the same method as in the previous section (i.e. the velocity Verlet method), and the dipole is evaluated analogously as well:

$$\mu(t) = \mathbf{Tr}[\mathbf{P}(t) \cdot \mathbf{d}]. \tag{3.15}$$

Ehrenfest dynamics is a nonadiabatic method, where coupling between the eigenstates arises from the time derivative couplings implicitly contained in the time-dependence in the electronic Hamiltonian that results from it being continually updated along the nuclear trajectory.[79] Therefore, Ehrenfest dynamics can describe nonradiative transitions in a natural fashion, so lifetime-based homogeneous broadening is recovered in the frequency-domain dipole correlation functions.

3.4 Vibrationally-resolved Absorption Spectra from Ehrenfest Dynamics

Ab initio calculation of electronic absorption spectra for isolated molecules has been a core motivation for the recent explosion in the development of highly accurate excited state electronic structure methods. Even for the most accurate of these approaches, though, it is still somewhat dissatisfying to overlay the “stick spectra” (i.e. the set of excitation energies and associated transition probabilities) they produce with the corresponding experimental, gas-phase spectra. Typically, one would reconcile the qualitative disagreement in the computed and experimental spectrum by convoluting the highly-accurate stick spectrum with some empirically motivated broadening function to account for the role that finite excited state lifetimes and nuclear motions play in determining the shapes of features in the absorption spectrum. In this chapter, however, the excited state lifetime and nuclear dynamics effects on the photoabsorption cross-section take the main stage, as we answer the question of whether vibrationally-resolved electronic absorption line-shapes can be predicted with time-domain simulations in which electrons are treated quantum mechanically with a mean-field (i.e. Hartree-Fock) description of their interactions, and the nuclei behave as classical point-charges in the average potential of the evolving electronic superposition. This approach is contrasted with the standard combined electronic/vibrational eigenstate transitions probabilities (i.e. line shapes derived from the Franck-Condon Principle), then analyzed in the context of a simple toy system comprised of a two-state electronic system modulated by a single (harmonic) vibrational mode. Finally, the method is preliminarily applied to a polyatomic system known to exhibit extensive vibronic sidebands in its gas-phase absorption spectrum, acetylene.

3.5 Vibronic Sidebands as Transitions between Vibrational Eigenstates within the Ground/Excited Electronic Energy Eigenstates

The treatment of the vibronic sidebands in the electronic absorption spectra of molecular systems has long posed a challenge for quantum chemists. Since, most often, nuclei are regarded as little more than the classical point-charges that determine the distribution of positive charge that binds the electrons, the nuclear part of the molecular wavefunction is almost universally an afterthought for electronic structure theorists.

Given the full Born-Oppenheimer approximate potential energy surface for a particular electronic state, the vibrational eigenstates can be resolved for that state's electronic potential. Excited state electronic structure methods are generally more expensive than their ground state analogues, so one cannot hope to exhaustively sample the full nuclear configuration space with discrete electronic energy calculations except for systems with very few degrees of freedom. The global potential energy surfaces for the electronic energy eigenstates, and therefore the eigenfunctions of the vibrational Hamiltonian that includes this global potential, can only be solved for approximately. The most common theoretical approaches for treating the vibronic sidebands in electronic absorption line shapes rely on resolving approximate vibrational energy eigenstates within the (often dubious) harmonic approximation, where the vibrational eigenstates are solved not for the true electronic potential, but for a second-order Taylor series of the true electronic potential expanded about the equilibrium geometry for each Born-Oppenheimer frame electronic energy eigenstate..[99–103]

Even in this drastically simplified situation, the complete set of all mixed partial second derivatives of the electronic potential (i.e. the Hessian of the electronic energy) with respect to the nuclear degrees of freedom is needed to solve for the harmonic normal modes and their associated harmonic force constants. For many high-level electronic structure theories, this will require the use of numerical differentiation methods, which becomes intractable for systems larger than just a few atoms. Nonetheless, once these quantities are known, the vibrational eigenfunctions within this approximation are simply those of the corresponding one-dimensional harmonic oscillator, and the overlap integrals between these states can be calculated analytically. This basic approach is at the heart of the current state of the art methods for determining the vibronic lineshapes from the combined electronic/nuclear eigenstate vantage.

In an effort to decrease the expense of these calculations, often times the "Condon approximation" is invoked, which takes the electronic dipole operator to be independent of nuclear configurations. This approximation, in combination with the electronic/nuclear eigenstate transition picture for vibronic transitions described above, defines the "Franck-Condon Principle" (FCP).[99,104] As can be intuited, the Condon approximation is not a good approximation for systems that undergo large-amplitude nuclear motions. One must account for at least the linear variations of the electronic dipole operator with respect to nuclear displacements in this case.

In spite of their potentially formidable expense, FCP lineshape calculations can fail to give reasonable results in a variety of different fashions. For systems with excited state equilibrium geometries that differ drastically from that of the ground state, one must often consider large vibrational quantum numbers for the ground-excited state vibrational eigenfunction overlap integrals to become nonzero. This can give nonsensical lineshapes, since the harmonic approximation likely no longer provides an adequate description of the vibrational eigenstates for such highly excited vibrational states. Furthermore, many vibrational motions (dihedral angle modifying torsional motions, for example) are poorly described by a harmonic potential even near to the equilibrium geometry.

The use of the harmonic approximation in FCP lineshape calculations isn't solely responsible for the failure of this approach to reproduce vibronic lineshapes though. There are intrensic problems with this approach when, for example, there is a change in the number of internal degrees of freedom of the molecule upon excitation (e.g. for HCCH, with a linear ground state minimum with sp hybridized carbons and a nonlinear excited state minimum with sp^2 carbons resulting from the $\pi \rightarrow \pi*$ valence excitation.)[105] Other times, the seemingly straight-forward step of excited state geometry optimization can be challenging, such as for systems with highly degenerate excited states like the permanganate ion.

Even when the Franck-Condon approach within the harmonic approximation doesn't fail outright, one must optimize the molecuar geometry subject to an excited state potential energy surface, and calculate the Hessian *for every excited state of interest.* So, even when the method can be used successfully, it can be extremely expensive if vibrational progressions for numerous electronic transitions are needed.

Beyond the aforementioned drawbacks, the FCP methods can only account for the ensemble effects, i.e. the "inhomogenous" broadening associated with the different nuclear states in the ground and excited electronic states. A more complete description of the absorption lineshape would result from some natural description of the lifetime broadening from the time-energy uncertainty relation. It seems that while it may be a convenient basis in which to *interpret* the coupled electronic-vibrational transitions that give rise to vibronic sidebands in absorption spectra, predicting the vibrationally-resolved lineshape directly in this time-independent fashion may not be an ideal approach for arbitrary molecular systems. A far more desirable situation would be to get all of this information from a single, mixed quantum/classical time-domain simulation of the molecular degrees of freedom.

3.6 The Dipole Correlation Function Approach to the Absorption Lineshape

There is an elegant alternative for computing the absorption lineshape that doesn't require the resolution of vibrational eigenstates for each electronic state, or even the electronic eigenstates themselves. Instead, a manifestly time-dependent approach is taken, in which an initial wavepacket is propagated, and spatial recurrences in its motion are tracked and transformed to the frequency domain to give the absorption spectrum.[8,106–108] This intuitive picture formally relies on the dipole-dipole correlation function, $C_{\mu\mu}$, to mathematically describe the recurrences of the wavepacket in time:

$$C_{\mu\mu} = \langle \Psi(0) | \hat{\mu}(0) \hat{\mu}(t) | \Psi(0) \rangle \tag{3.16}$$

where $\mu(t) = e^{i\hat{H}t/\hbar}\hat{\mu}e^{-i\hat{H}t/\hbar}$. The photoabsorption cross-section, $\sigma(\omega)$, is then proportionate to the Fourier transform of $C_{\mu\mu}$:

$$\sigma(\omega) \propto \omega \,\mathrm{Re} \int_0^\infty e^{i\omega t} C_{\mu\mu}(t) dt. \tag{3.17}$$

The correlation function approach to the photoabsorption cross-section has a long history in the simulation of IR spectra.[109] This approach is straight-forward to apply in this case, because classical molecular dynamics (MD) will give non-zero velocity for each of the vibrational modes even in the zero temperature limit according to their zero point energies. So, the dipole signal extracted from a MD simulation initialized with at least the zero-point vibrational energy accounted for in the initial conditions will be non-stationary even for simulation of systems in their ground electronic and vibrational states. This will be the case for classical molecular dynamics regardless of which state (or states) are contributing the forces on the classical nuclei. The correlation function approach is, therefore, well-suited for resolving the absorption spectrum from the Ehrenfest, or mean-field mixed quantum-classical MD simulations.

Many practitioners of quantum electronic dynamics have used an explicitly time-dependent approach similar in spirit to the correlation function based approach described here to compute absorption cross-sections (with lifetime broadening effects) using RT-TDSCF based methods.[110] In this case, the frequency dependent polarizability is the quantity used to determine the lineshape rather than the dipole-dipole time correlation function.[111] When an impulsive (i.e. δ-spike) electric field is applied to the system, an electronic wavepacket with contributions from each of the energy eigenstates is formed, and the polarizability tensor (the trace of which is proporional to the absorption cross-section) can be computed from the frequency-domain representations of the dipole evolution and the applied electric field by:[96,112]:

$$\mu_i(\omega) = \alpha_{ii}(\omega) E_i(\omega) \tag{3.18}$$

where α is the dipole-dipole polarizability tensor, E is the applied electric field, and i is a spatial component index. To those who have used this approach with the RT-TDHF/DFT methods, the correlation-function based approach may appear to be a departure from the literature on the topic of computing absorption spectra. Recall, though, that with the Ehrenfest dynamics, the electronic degrees of freedom will naturally evolve into a superposition state through the coupling brought about by nuclear motions and the non-diagonal nature of the nuclear momentum operator in the basis of Born-Oppenheimer frame energy eigenstates. In this case, there is no need to further perturb the system with an external field to observe the dipole-allowed transitions in the correlation-function based absorption cross-sections that derive from the Ehrenfest dynamics. The absorption cross-section in this case can be defined in terms of the frequency domain dipole-dipole autocorrelation function (Eq. (3.17),) with no need to account for the effect of any external perturbation on the dipole time evolution. Note that the same is not true in the case of RT-TDHF/DFT with static nuclei, where no change in the dipole moment would be expected for a system initialized in its electronic ground state, since the initial state is in this case a solution to the time independent Schrödinger equation and is therefore a stationary state for that nuclear configuration. However, it should be noted that correlation function based theories are couched in a perturbative treatment of the rate at which the system absorbs energy from the incident field, which leads to expressions for the photo-absorption cross-section which depend solely on the field-free dynamics. That is, the absorption line-shape function carries no explicit dependence on the applied field, preventing any description of vibrational effects on important higher order optical processes. The more general approach to the absorption lineshape is provided through the frequency dependent molecular polarizability. Identifying the origins of resonances that contribute to its pole structure will help answer the question of which spectral features can be captured using the Ehrenfest approach.

In contrast to the FCP-based approach, the correlation function methods based on molecular dynamics utilize the full (anharmonic) potential energy surfaces, and explicitly account for the variation in the electronic dipole operator with respect to nuclear motions. Also, the full spectrum can theoretically be resolved from a single (sufficiently long) molecular dynamics simulation. With these benefits in mind, we move to the methodological sections describing the Ehrenfest dynamics implementations in both the single-particle (orbital) basis and a truncated basis of many-body electronic energy eigenstates.

3.7 Analytical Behavior of the Two-Level System Coupled to a Harmonic Vibrational Mode

While the vibronic sidebands can be explained formally as transitions between combined electronic and nuclear energy eigenstates in the FCP picture, it is noteworthy that there exists earlier work on the topic that relies purely on a classical description of the nuclei.[113] Consider, as an illustrative example, a diatomic system with electronic structure modeled by a simple two-level system with energy gap $\hbar\omega_e$. Suppose that the splitting between these two levels is modulated by the changing nuclear potential experienced by the electrons along the diatomic's stretching mode, which causes periodic oscillation of the bond length with frequency ω_n. This will cause a time-dependent modulation of the molecular dipole moment, such as that observed in Sec. 3.8. For this simple system, we can express the time evolution of the molecular dipole moment by:

$$\boldsymbol{\mu}(t) = \cos(\omega_e t + B\sin(\omega_n t)) \tag{3.19}$$

In Eq. (3.19), B determines the strength of the dipole modulation by the nuclear vibration, and is generally less than unity. It is possible to express Eq. (3.19) as a sum over the sperical Bessel functions (of the first kind) to do away with the dependence of the expression on $sin(\omega_n t)$:

$$\boldsymbol{\mu}(t) = \sum_{m=-\infty}^{\infty} J_m(B)\ \cos((\omega_e + m\omega_n)\, t) \tag{3.20}$$

Fourier transformation of Eq. (3.20) gives a dipole spectrum with peaks at $\omega_e \pm m\omega_n$ for all integers m, with corresponding intensities given by $J_m(B)$. However, for small B, $J_m(B)$

quickly approaches zero for large $|m|$, so only a finite number of sidebands are observable in the spectrum. The intensities of the sidebands are ultimately determined by the coupling strength, B, with large coupling giving a greater number of vibronic transitions visible in the spectrum. Note that B is related to the ratio of the change in the electronic dipole at the most-stretched configuration to the frequency of the nuclear vibration.[114] So, the value of B depends fundamentally on the intrinsic "vibronic" coupling between the nuclear and electronic degrees of freedom, but can also be affected by the amplitude of the nuclear vibration.

Identifying the Origin of Poles in the Frequency Dependent Polarizability

Consider the time-dependent electric dipole $\boldsymbol{\mu}(t)$ of a system evolving under the influence of a weak electric field (e.g. linear response) and undergoing motion along some normal mode coordinate R. In the case where R is stationary, the time-dependent dipole is given as

$$\boldsymbol{\mu}(t) = \boldsymbol{\mu}(0) + (\boldsymbol{\alpha} * \boldsymbol{E})(t) \tag{3.21}$$

where $\mu(0)$ is the dipole moment for the reference state (e.g. the ground state) at the (field-free) equilibrium geometry, $\boldsymbol{\alpha}(t)$ is the time-dependent polarizability and $\boldsymbol{E}(t)$ is the time-dependent external electric (dipole) field. In the above equation, $(\boldsymbol{\alpha} * \boldsymbol{E})(t)$ is the convolution of the time-dependent polarizability and the applied field. The Cartesian components of time-dependent polarizability tensor can be written as a sum over electronic states

$$\alpha_{ij}(t) = \Theta(t) \sum_{n(\neq 0)} \langle 0|\hat{\mu}_i|n\rangle\langle n|\hat{\mu}_j|0\rangle \sin(\omega_{0n} t) \tag{3.22}$$

where $\Theta(t)$ is the Heaviside step function and ensures causality of the response. The system has electronic resonances at frequencies ω_{0n} with magnitudes governed by the absolute squared transition dipole, $|\langle 0|\hat{\mu}_i|n\rangle|^2$.

Assuming an impulse electric field is applied along Cartesian direction j with intensity

E_j, the i component response of Eq. (3.21) can be rewritten as

$$\mu_i(t) = \mu_i(0) + \alpha_{ij}(t) \cdot E_j \tag{3.23}$$

If we expand Eq. (3.23) in terms of displacements of R about its equilibrium value, R_0, to first order we have

$$\mu_i(t) = \mu_i(0) + \alpha_{ij}(t) \cdot E_j + \frac{\partial \mu_i(0)}{\partial R}(R - R_0) + \frac{\partial \alpha_{ij}(t)}{\partial R} E_j (R - R_0) + \cdots \tag{3.24}$$

Here, R is parameterized by t, though we leave the explicit t dependence off for clarity. We can replace the $R - R_0 \rightarrow \Delta R \cos(\omega_N t)$ by making the observation that for small displacements from R_0, the normal mode coordinate will evolve nearly harmonically with a maximum displacement ΔR. Making this substitution and moving $\boldsymbol{\mu}_0$ to the left gives

$$\mu_i(t) - \mu_i(0) = \Delta\mu_i(t) = \alpha_{ij}(t) \cdot E_j + \frac{\partial \mu_i(0)}{\partial R}[\Delta R \cdot \cos(\omega_N t)] + \frac{\partial \alpha_{ij}(t)}{\partial R} E_j [\Delta R \cdot \cos(\omega_N t)] + \cdots \tag{3.25}$$

Taking the Fourier transform of the above Eq. (3.25) and assuming positive frequencies, we have

$$\begin{aligned} \Delta\mu_i(\omega) \propto E_j \cdot & \sum_{n(\neq 0)} [\langle 0|\hat{\mu_i}|n\rangle\langle n|\hat{\mu_j}|0\rangle]\delta(\omega_{0n} - \omega) \\ & + \Delta R \cdot \frac{\partial \mu_i(0)}{\partial R}\delta(\omega - \omega_N) \\ & + \Delta R \cdot E_j \cdot \sum_{n(\neq 0)} \frac{\partial}{\partial R}[\langle 0|\hat{\mu_i}|n\rangle\langle n|\hat{\mu_j}|0\rangle]\delta(\omega_{0n} \pm \omega_N - \omega) + \cdots \end{aligned} \tag{3.26}$$

From this we can see that the first term corresponds to pure electronic transitions at the equilibrium geometry, which are routinely obtained in frozen nuclei RT-TDSCF. The second term accounts for spectral features arising from the ground state dipole moment changing with respect to vibration along a normal mode. These are the infrared (IR) allowed transitions corresponding to vibrational frequency ω_N, and is analogous to the treatment of IR spectra in classical molecular dynamics. Finally, the last term gives how the polarizability changes with respect to vibration along a normal mode. These are the so-called Herzberg-Teller terms in the vibronic theory of resonance Raman intensities, and account for the Raman-allowed transitions resulting from coupling between electron transitions and vibrational motion. Accordingly, they take a very similar form to the "B" term in Albrecht's seminal work on Raman intensities.[115–117] Unlike Raman spectroscopy, the Ehrenfest protocol is energy conserving, so it does not permit de-excitations, and the Raman transitions appear only as sidebands of the electronic transitions. Although we have neglected higher-order terms in the above derivation, it is easy to extend the above procedure to higher orders in ΔR and obtain classical combination and overtone bands. In the *ab initio* simulations, though, the response of the dipole moment to all orders in the vibrational displacements (i.e. beyond the Herzberg-Teller term) and impulsive field strength are captured explicitly, so contributions to the spectral lineshape arising from these higher order terms are resolved with no added complexity, in contrast to the time-independent approaches.

3.8 Application to Vibrationally Resolved Absorption Spectra of Small Molecular Species

H_2 Absorption Spectrum from Field-Free Ehrenfest Dynamics

In order to see the long-time behavior for a small model system, in this section we show the results of performing the Ehrenfest dynamics in the basis of electronic energy eigenstates resolved using configuration interaction with single excitations (Hartree-Fock reference determinant, STO-3G basis). 250,000 numerical integration steps with a stepsize of ∼1.2 as (0.5 atomic unit of time) were carried out for a series of differently stretched H_2 molecules, all started with zero initial velocity (i.e. at the classical turning points in the nuclear dynamics) All dipole, potential, and nonadiabatic coupling matrix elements were resolved by a fine-resolution scan of the H-H bond, and interpolated. The photoabsorption cross-sections (Eq. (3.17)) were evaluated for each, and are plotted on equally-scaled axes in Sec. 3.8.

HCCH Absorption Spectrum from Field-Free Ehrenfest Dynamics

In this section, we demonstrate the power of the general, density matrix propagation based Ehrenfest dynamics code to generate vibrationally resolved absorption spectra. Here, 200 fs of nuclear dynamics with an electronic time step of 1 as and nuclear time step of 100 as was used to generate the absorption cross-sections plotted in Sec. 3.8. Initial conditions were generated by accounting only for the zero-point vibrational energies of the normal modes, and taking the phase along the vibrational modes to be random.

H_2/D_2 Isotope Effects in the Vibrationally Resolved Spectrum using Frequency Dependent Polarizability Following Weak Impulsive Electric Field Perturbation

In order to illustrate the contributions of nuclear motion to the Ehrenfest description of electronic sidebands, we first consider two simple systems, H_2 and D_2 at the RT-TDHF/STO-3G level of theory. All calculations were performed using the development version of the Gaussian electronic structure software[98]. After distorting the geometry slightly (*vide infra*) we perturb with a weak delta electric field corresponding to a strength of 0.0001 au polarized along the bond axis (z-component). This field is sufficiently weak so as to keep the Ehrenfest potential effectively in the ground state, and we cannot find any evidence of strong state mixing in the dynamics, evidenced by ω_N remaining in the ground state vibrational mode. The Ehrenfest equations of motion were integrated with electronic and nuclear time steps of 0.0012 fs and 0.0036 fs. These are relatively short time steps, chosen to ensure the smooth co-evolution of electrons and nuclei. Simulations were run for 50 fs and the z-component of the time-dependent dipole moment was Fourier transformed using the Padé approximant scheme[118] which gives high-resolution spectral data with relatively short simulation times. This Fourier transform is proportional to the dipole strength function for isotropic samples. Here we plot only the magnitude of the real component of the frequency-multiplied Fourier transform, which corresponds to absorptive line-shapes. The imaginary component has the same pole and intensity information, but the line-shape is dispersive. The two contain identical information and are related *via* the Kramers-Kronig relations[119]. Though the 50 fs simulation time may appear small, it is more than sufficient to capture vibrational effects when used with the Padé approximant Fourier transform scheme. We have investigated longer time behavior of the systems (out to 300 fs, data not shown) and cannot detect any noticeable change in the resulting absorption spectrum.

For the minimal basis RHF/STO-3G H_2 and D_2, the systems have one bright electronic transition at $\omega_{0n} = 26.21$ eV at an equilibrium bond length of 0.7122 Å. H_2 has one vibrational mode $\omega_N = 0.69$ eV while D_2 has its $\omega_N = 0.48$ eV, which are related by a factor of $\sqrt{2}$ on account of the higher mass of deuterium. Starting with the nuclei at a slightly compressed initial bond length (0.7100 Å) for each system and then perturbing with the weak delta-like pulse, the electronic and vibrational dynamics were allowed to co-evolve within the *ab initio* Ehrenfest method.[78] The obtained optical absorption spectra are given in Fig. 3.4. Here, we can clearly see that both systems have a strong pure electronic absorption at 26.21 eV. However, over the course of the dynamics, the vibrational-frequency modulated electric dipole moment gives rise to very different line-shapes. From merely allowing the nuclear positions of these isotopologues to evolve classically, the vibrational nature of the sidebands is revealed through their spacings, which are related to each other by a factor of $\sqrt{2}$; a clear isotopic effect. Although not shown, there is no transition in the infrared region, which is to be expected as H_2 and D_2 have no ground state dipole moment and direct photo-excitation of the stretch is not dipole allowed. However, the stretch is Raman-active, so we observe the Raman sidebands around the electronic transition.

H_2 and CO Spectrum from Frequency Dependent Polarizability with Impulsive Electric Field Perturbation

Finally, we show a slightly more realistic system with a non-zero ground state dipole moment, CO at RT-TDHF/6-31+G*, to illustrate how, in one shot, the Ehrenfest approach obtains both electronic excited state information as well as ground state vibrational information. The bond length was compressed by 0.01 Å from the optimized ground state geometry of

1.1133 Å to 1.1033 Å. The simulated spectrum is given in Fig. 3.5. We can see a fairly strong IR peak at 0.30 eV, which corresponds to the CO stretch obtained from an optimization and frequency calculation on the same system. Furthermore, we see the first overtone at 0.60 eV, with a far smaller intensity due to the $(\Delta R)^2$ dependence. Though the overtones appear quantum, we could not find evidence of quantum anharmonic corrections to these peaks, so it appears these overtones are due to the classical treatment of the nuclei. If they were quantum in nature, we would not expect the overtones to be integer multiples of the fundamental frequency, which is what we observe. All of the bright electronic transitions further up in energy display sidebands separated by the 0.30 eV vibrational frequency. Because CO is of the point group $C_{\infty v}$, the CO stretch is both IR and Raman active.

In conclusion, we have shown that extending the traditional RT-TDSCF approach to computing absorption spectra to include vibrational motion in the mixed quantum-classical Ehrenfest approach does in fact encode the effects of vibrational transitions into the electronic absorption spectrum, evidenced through isotopic effects and dependence on geometric displacement. In contrast to classical MD simulations, here we have shown that the Ehrenfest mixed quantum-classical dynamics captures vibrational effects on electronic absorption spectra. In particuar we see Raman sidebands corresponding to Herzberg-Teller terms which is a strictly quantum vibrational effect. This extends the utility of the Ehrenfest approximation to new classes of spectroscopic phenomena inaccessible to classical MD simulations, and opens up new avenues of interesting research with mixed quantum classical approaches.

Conclusions & Perspective

In this chapter, we have shown support for the suitability of the Ehrenfest method to predict the vibrationally-resolved electronic absorption spectral features from first principles. The resulting spectra were interpreted in light of a simple analytical model introduced before the wide-spread adoption of quantum physics nearly a century ago. Future work in this direction will apply the method to larger systems with a more accurate treatment of the electronic system (i.e. higher level of theory), and compare the resulting spectra with published experimental spectra with well-resolved vibronic sidebands.

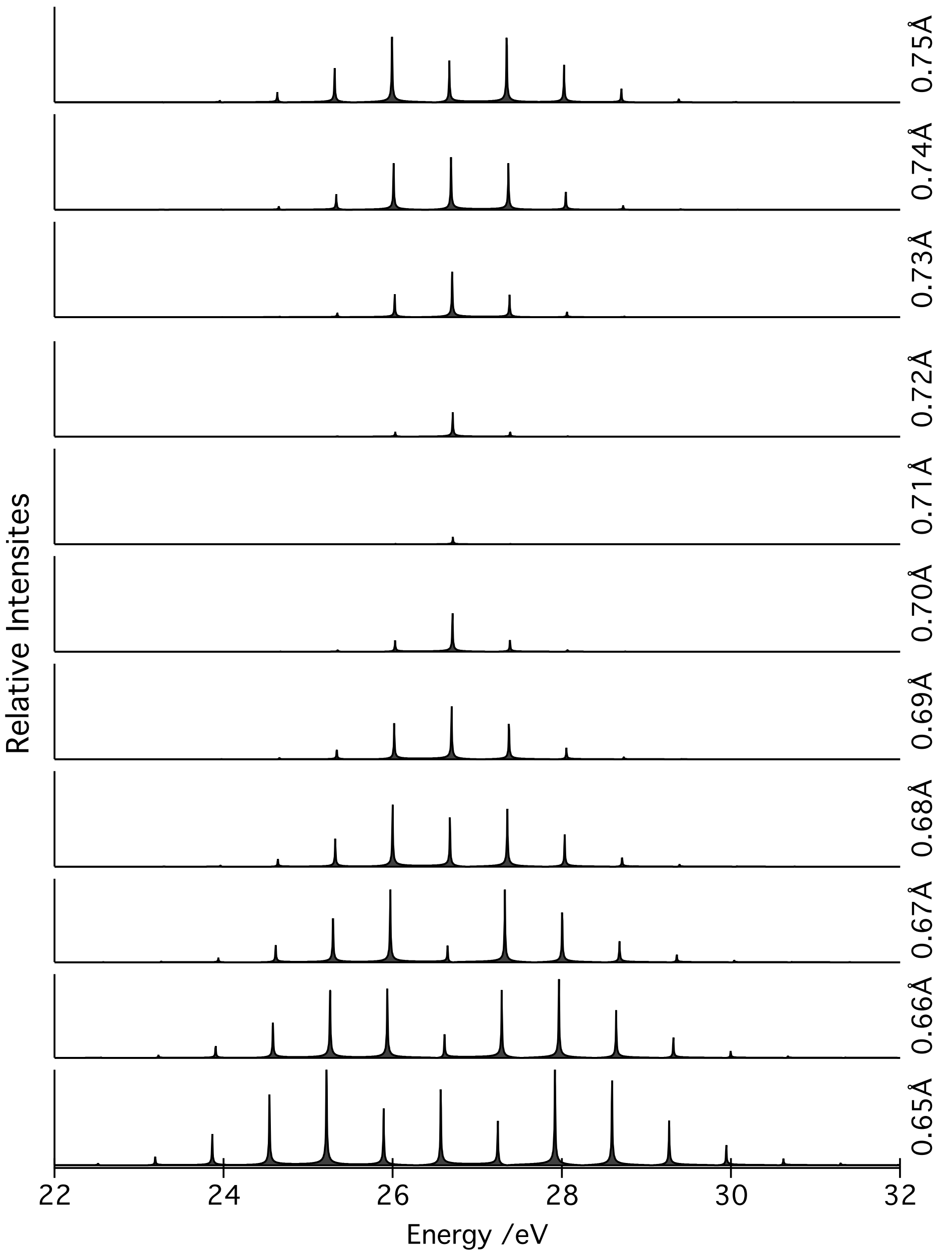

Figure 3.1: Vibrationally-resolved electronic absorption spectra (plotted on identically scaled axes for ease of comparison) for H_2 started from a range of different bond lengths (zero initial velocity, so classical turning points in the nuclear dynamics.) Note that the equilibrium bond distance is ~ 0.71Å at this level of theory, so a loss of intensity here occurs from a lack of nuclear motion and, therefore, mixing of the energy eigenstates.

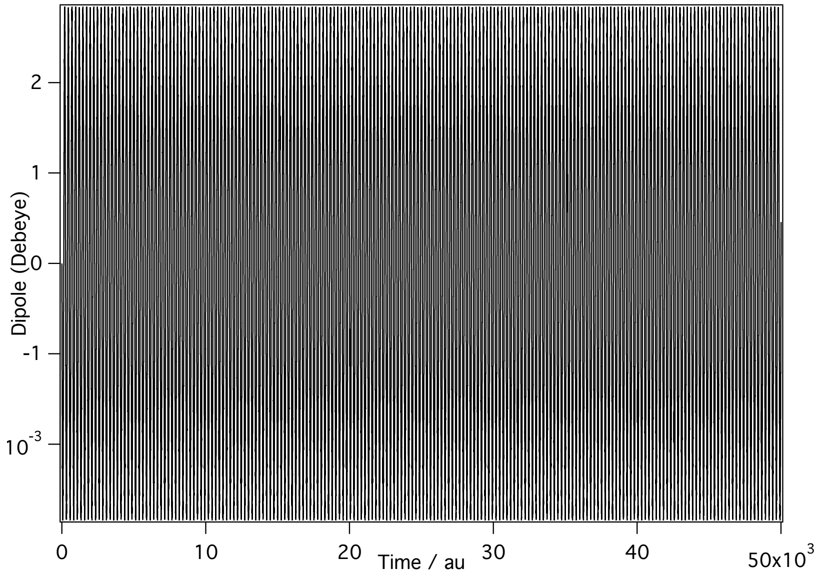

Figure 3.2: Dipole evolution for the 0.65 Å stretched H_2 molecule within a truncated (2-state) expansion of the electronic wavepacket, demonstrating a small, periodic modulation of the dipole oscillation frequency with a timescale characteristic of the H_2 stretch.

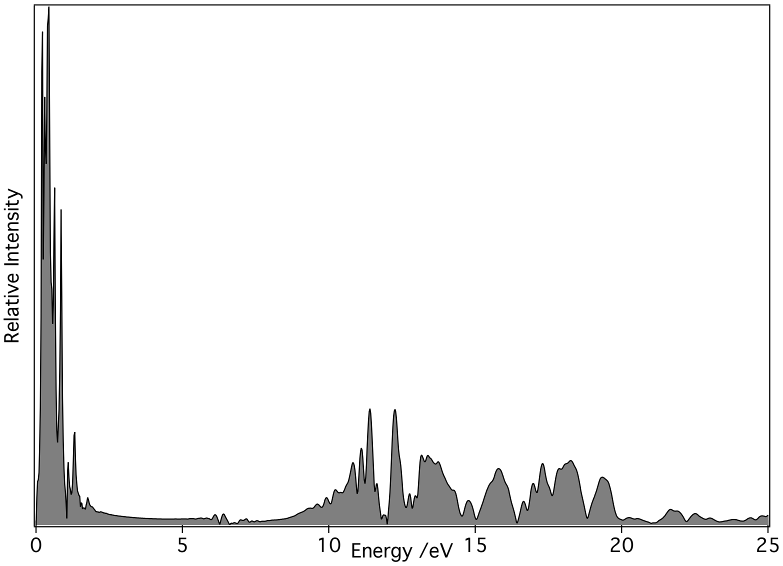

Figure 3.3: Vibrationally-resolved absorption spectrum (from IR to VUV) from a single 200 fs trajectory computed using the single-particle basis Ehrenfest implementation in the Gaussian suite of programs.

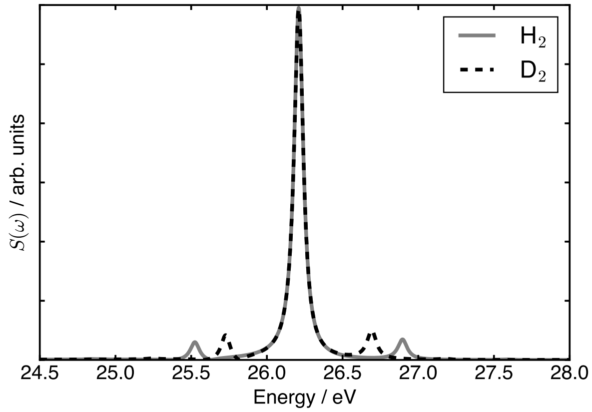

Figure 3.4: Computed optical absorption spectra of H_2 and D_2 using the Ehrenfest dynamics approach at the RT-TDHF/STO-3G level of theory. Each molecule was displaced from its equilibrium bond length of $R = 0.7122$ Å to a slightly shorter bond length of $R = 0.7100$ Å (maximum displacement of 0.0022 Å). Theoretically, D_2 sidebands should be $\sqrt{1/2}$ eV less than those of H_2, which is observed here. $\omega_N^{H_2} = 0.69$ eV and $\omega_N^{D_2} = 0.48$. Because displacement is small, the intensity of the central peak and sidebands is dominated by the first order terms. Thus, it is possible to see $\omega_e \pm 2\omega_N$ sidebands, though they are vanishingly small. Reproduced with permission from reference 2.

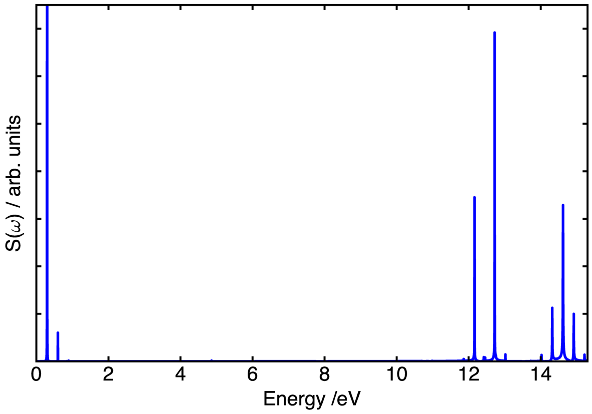

Figure 3.5: Computed optical absorption spectra of CO using the Ehrenfest dynamics approach at the RT-TDHF/6-31+G* level of theory. Here we perturb along the bond axis z so only z-allowed dipole transitions are shown. Furthermore, the bond is stretched from equilibrium by 0.01 Å. The CO stretch is visible at 0.30 eV, and a slight first overtone is visible at 0.60 eV. The higher-energy Raman transitions have sidebands separated by the ground state CO stretch frequency of 0.30 eV. Reproduced with permission from reference 2.

Chapter 4

SHORT-TIME ELECTRONIC DYNAMICS SIMULATIONS WITH FROZEN NUCLEI

4.1 Introduction to RT-TDDFT

In this chapter, the “real-time” (RT) variant of time-dependent density functional theory (TDDFT) will be presented and contrasted with the more commonly applied linear-response perturbative variant, (LR-TDDFT). The presented methods will then be applied to model and interpret electronic coherences in selected binuclear complexes.

The LR-TDDFT approach has risen to prominence in the *ab initio* treatment of electronically excited states due to its generally favorable cost/accuracy ratio.[63,74,120–128] At the same time, the fundamental approximations typical of practical TDDFT implementations have been studied, and their implications are becoming increasingly well-understood.[129,130] Historically, Yabana and Bertsch were first to implement RT-TDDFT electron dynamics, and applied the method to the calculation of linear absorption spectra of small metal clusters.[68] However, the generality of the approach quickly lead to its adoption by theoreticians studying a variety of electronic processes occurring on the ultrafast (typically sub-picosecond) timescale[131], including time-resolved electronic absorption for modeling transient spectroscopies[132,133], charge transfer in photovoltaic materials,[134–136] charge carrier dynamics in semiconducting nanomaterials[137,138], electronic stopping of ballistic ions,[139] and the evolution of quantum-coherent plasmonic states in metal nanowires.[140,141] RT-TDDFT propagates a superposition of electronic states by integrating the time-dependent Kohn-Sham equations in the Liouville–von Neumann form. From the RT-TDDFT results one may gauge the extent to which a system may support a long-lived excited state electronic coherence. Since the RT-TDDFT method is now a well-established and widely applied method, we present only the most pertinent details of our implementation and refer readers to our earlier publications for a more complete description of the method.[78,138,142,143]

The time-dependent Kohn-Sham equations can be expressed as

$$i\frac{\mathrm{d}\mathbf{P}(t)}{\mathrm{d}t} = [\,\mathbf{K}(t), \mathbf{P}(t)] \tag{4.1}$$

where $\mathbf{P}$ and $\mathbf{K}$ are the density and Kohn-Sham matrices in an orthonormal basis. The modified midpoint and unitary transformation (MMUT) algorithm is used to propagate the density in time

$$\mathbf{P}(t_{n+1}) = \mathbf{U}(t_n) \cdot \mathbf{P}(t_{n-1}) \cdot \mathbf{U}^{\dagger}(t_n). \tag{4.2}$$

The unitary time evolution operator $\mathbf{U}(t_n)$ is constructed from the eigenvectors (columns of $\mathbf{C}$) and eigenvalues ($\{\epsilon_i\}$) of the Kohn-Sham matrix

$$\begin{aligned} \mathbf{U}(t_n) &= \exp\left[-2i\,\Delta t\,\mathbf{K}(t_n)\right] \\ &= \mathbf{C}(t_n) \cdot \exp\left[-2i\,\Delta t\,\boldsymbol{\epsilon}(t_n)\right] \cdot \mathbf{C}^{\dagger}(t_n), \end{aligned} \tag{4.3}$$

The time-dependent dipole moment can be evaluated as,

$$\mu(t) = \mathrm{Tr}[\mathbf{P}(t) \cdot \mathbf{d}] \tag{4.4}$$

where $\mathbf{d}$ is the dipole matrix in orthonormal basis.

During the electronic dynamics, the time evolving density matrix can be transformed into the basis of the time-zero molecular orbitals

$$n_{ij}(t) = \mathbf{C}_i^{\dagger}(0) \cdot \mathbf{P}(t) \cdot \mathbf{C}_j(0). \tag{4.5}$$

The diagonal elements from Eq. (4.5) correspond to changes in orbital occupation and the off-diagonal elements track coherences between different orbitals.[144] In this current work, these simulations use frozen nuclei, so there is no mechanism to transfer energy from the electronic to the nuclear degrees of freedom. Since only the short-time evolution of the electronic state in the singlet manifold is considered in this work, the pertinent low frequency Pt–Pt stretching mode that most dramatically modulates the S_1/S_2 splitting will undergo only a fraction of a period of oscillation over the duration of our simulations. In this case, fixing the nuclei at the Franck-Condon geometry should not substantially modify the early electronic dynamics following the electronic perturbation. This also removes nuclear motion as a possible dephasing mechanism for the prepared superposition state. Nevertheless, electronic coherence/decoherence as a result of interference between different electronic states can be observed with the RT-TDDFT method.

Coherent superpositions of low-lying electronic states were prepared in the studied systems by first identifying the pair of adiabatic molecular orbitals (one occupied, one unoccupied) that most strongly contributes to the transition densities for the lowest spin-allowed excitations using LR-TDDFT. The corresponding single particle excitation is then enacted on the ground state wave function at the start of the simulation. In this way, electronic wavepackets dominated by these lowest-lying energy eigenstates can be systematically prepared. See the "Quantum Electronic Dynamics Simulations" Section for details on the initial state preparation.

All calculations were performed using the crystal structure geometries with fixed nuclear positions. Crucially, this allows for the pure electronic dephasing/interference effects to be isolated from those induced by the nuclear motions. Since range-corrected functionals more accurately describe charge transfer electronic states like those at the center of this work, the CAM-B3LYP functional[145] and LANL2DZ basis set[146,147] were used to model all complexes. All calculations were performed in a development version of the Gaussian software package.[98]

4.2 Application to Modeling Excited State Coherence in Binuclear Platinum Complexes

Coherent electronic energy transfer has been implicated in some of the most efficient energy and charge transport pathways in nature, providing a well-defined means of controlling and directing energy flow.[148–150] Molecular systems exhibiting relatively long-lived electronic coherence represent a potential route to achieve high quantum efficiencies for exciton splitting/transport in photovoltaic devices and are integral components to the development of quantum computing.[151] Materials that can support the long-lived phase coherence required to facilitate coherent transport are becoming important to a range of pure science disciplines and technological applications, and among them, systems with multi-metal centers are interesting candidates to study these effects, especially those complexes which undergo multielectron transfer processes.[3,152,153]

System	Pt–Pt (Å)	$\angle_{(\text{Pt–Pt-ppy})}$ (deg.)
1	3.27	122.871
2	3.23	117.780
3	2.98	115.466
4	2.91	106.028

Table 4.1: Summary of the pertinent geometric variables extracted from the crystal structure geometries of **1–4**. Pt–Pt-ppy angles are calculated as an average value between the two platinum centers and the ppy ligand's nitrogen.

Binuclear Pt(II) complexes have recently been identified as molecular systems that hold potential to exhibit sustainable excited state electronic coherence.[3] The complex is comprised of two pseudo two-fold symmetry related square-planar subunits that create metal–metal $d\sigma$ bonding and $d\sigma^*$ antibonding orbitals from overlapping $5d_{z^2}$ orbitals on the platinum atoms (Fig. 4.1). Pyrazolate (pz) ligands functionalized with various substitutional groups at the 3- and 5- positions bridge the Pt atoms, which are also coordinated by bidentate 2-phenylpyridine (ppy) ligands to form a rigid "A-frame" type structure. Several compounds with the same root structure, $[(\text{ppy})\text{Pt}(\mu\text{-R}_2\text{pz})]_2$, have been synthesized and characterized both experimentally and computationally (Fig. 4.1).[154] The steric bulkiness of the different substituents R = H (**1**), Me (**2**), ^{t}Bu (**3**), and Ph (**4**) on the pyrazolate bridging ligand changes the degree of separation and orientation of the two ppy ligands, as well as the inter-Pt distances (Tab. 4.1). Note that the structural parameters reported in Tab. 4.1 were resolved crystallographically, and therefore deviate somewhat from previously published, solution-phase structural parameters inferred from transient X-ray absorption photoelectron scattering data.[155]

Previous studies have shown that the electronic structure of the low-lying valence states can be effectively tuned by changing the substituents at the 3- and 5- positions of the pyrazolate. For complexes **3** and **4** with short Pt–Pt separations, the lowest energy electronic transitions are metal–metal-to-ligand charge transfer (MMLCT) in nature.[154] These are predominantly described as transitions from the $d\sigma^*$ (HOMO) to the in-phase (LUMO) and out-of-phase (LUMO+1) Pt+π^* orbitals (Fig. 4.1). The two sides (henceforth "left" and "right") of the binuclear complexes are coupled directly through Pt–Pt σ bonding, and π-interactions between the ppy ligands. In this strong coupling case, the electronic degrees of freedom of the whole complex respond to incident radiation as a single chromophore. At longer separations (complexes **1** and **2**), though, the two halves of the system areonly weakly coupled (if at all), and the first few electronic transitions are a mixture of ligand-centered (LC) and metal-to-ligand charge transfer (MLCT) transitions.[156,157] The left and right sides of the weakly coupled system respond to electromagnetic perturbation in much the same way that molecular crystals with multiple (identical) molecules per unit cell do. The isolated chromophores' degeneracies are removed in the condensed phase via a phenomenon known as Davydov splitting[158], where the extent of the level splitting is determined by the interaction strength between chromophores. The lowest energy electronic transitions in the structure with the longest Pt–Pt distance, **1**, are LC/MLCT due to the hybridization of the Pt d orbitals with the ligands. The methyl substituted complex **2** is intermediate of the other structures and exhibits both MMLCT and LC/MLCT transitions.

Being able to strategically and synthetically modify the excited state electronic structures makes these bi-nuclear complexes a unique platform for studying the physical underpinnings that control excited state electronic coherence.[154] It is yet to be determined what role the differing character of the energy eigenstates for **1** through **4** can play in determining their potential to support long-lived coherent electronic motions between the left and right halves of the complex. There are several requirements a system must meet for this phenomena to be observed in transient absorption anisotropy: two eigenstates must be simultaneously excited, the oscillatory period of the charge transfer must be shorter than the dephasing time, and the transition moments from the ground state to each of the two excited eigenstates must have different orientations.[159,160] From fundamental time-dependent theory for two-state systems, the frequency of the electron transfer is proportional to the splitting between the states. This simplified model is presented in Fig. 4.2, with the frequency of the oscillation identified as $2V_c$ where V_c is defined as the coupling strength between the two states. Since the Pt–Pt separation distance is the most pertinent structural factor that modulates the splitting energy, $2V_c$, we expect to see different periods of oscillation for these complexes that are dependent upon this distance. In this study, we directly simulate the electronic evolution of a coherent superposition of low-lying states in molecular complexes **1** through **4** using *ab initio* quantum electronic dynamics. The electronic interactions responsible for collapsing the excited state electronic coherence are analyzed from the perspective of a three state model Hamiltonian.

Results and Discussion

Excited State Energies and Couplings

Recurrent, coherent excitonic dynamics can be generally understood from the perspective of electronic couplings of molecular diabatic states. Consider the following effective three-state interaction Hamiltonian,

$$\mathbf{H} = \begin{pmatrix} \langle E_{left} \rangle & V_c & V_B \\ V_c & \langle E_{right} \rangle & V_B \\ V_B & V_B & \langle E_B \rangle \end{pmatrix} \tag{4.6}$$

where $\langle E_k \rangle$ is the energy expectation value for the k^{th} state, $\langle \phi_k | \hat{H} | \phi_k \rangle$. For our model system, ϕ_{left} and ϕ_{right} are electronic wave functions localized on fragments of a molecular complex according to Fig. 4.3, and all remaining states (referred to collectively as ϕ_B) are considered a "bath" to the ϕ_{left} and ϕ_{right} diabats. V_c and V_B are the electronic couplings between ϕ_{left} and ϕ_{right},

$$V_c = \left\langle \phi_{left/right} \right| \hat{H} \left| \phi_{right/left} \right\rangle , \tag{4.7}$$

and between ϕ_{left}/ϕ_{right} and ϕ_B,

$$V_B = \left\langle \phi_{left/right} \middle| \hat{H} \middle| \phi_B \right\rangle . \tag{4.8}$$

By symmetry, $\langle \phi_{right} | \hat{H} | \phi_B \rangle = \langle \phi_{left} | \hat{H} | \phi_B \rangle$. Diagonalization of Eq. (4.6) results in adiabatic states like those computed in most electronic structure methods.

From the perspective of time-dependent quantum mechanics, the coherence of a pure state as a linear combination of ϕ_{left} and ϕ_{right} will give rise to oscillatory behaviors of a quantum mechanical observable oscillating at $\omega \approx 2V_c$ (see Fig. 4.2).[161] If the coupling V_B between such a coherent subsystem and the rest of the system is zero, the coherent oscillation will last perpetually. However, in a realistic molecular system, such as those studied here, couplings between different diabatic states are non-zero. As a result, wave interference will usually impose limits on the lifetime of coherences in sub-systems on the manifold of electronic states (e.g. coherence between ϕ_{left} and ϕ_{right}). However, if the relative strength between V_c and V_B can be chemically tuned through synthetic modifications to enforce that $V_c \gg V_B$, such molecular systems have the potential to support long-lived coherent superpositions of the strongly coupled electronic states.

System	Pt–Pt (Å)	ω ($S_0 \rightarrow S_1$) (eV)	ω ($S_0 \rightarrow S_2$) (eV)	$\Delta E(S_2 - S_1)$ (eV)	${}^{V_c}/_{V_B}$
1	3.27	3.5203 (0.0685)	3.5821 (0.0125)	0.062	0.013
2	3.23	3.5113 (0.0832)	3.6001 (0.0222)	0.089	0.018
3	2.98	2.9140 (0.0591)	3.1641 (0.0096)	0.250	0.122
4	2.91	2.9297 (0.0562)	3.2538 (0.0082)	0.324	0.197

Table 4.2: Linear response TDDFT results for the first two excited states of **1**-**4**, including excitation energies (ω), oscillator strengths (in parentheses), S_1–S_2 splittings, and electronic coupling strength ratios ${}^{V_c}/_{V_B}$.

Table 4.2 shows the linear response TDDFT energy levels of photoexcited (adiabatic) states in molecular complexes **1-4**, and the corresponding electronic natural transition orbitals (NTO)[162] of the S_1 and S_2 states are plotted in Fig. 4.4. The S_1–S_2 gaps were also calculated for **1-4** using functionals which include varying amounts of exact Hartree-Fock exchange with the (semi-)local, DFT-type exchange, different forms of the exchange-correlation functional, and other range-separated hybrid functionals with different range cutoff parameters (see Supporting Information.) The qualitative trend of increased splitting of these levels with decreasing Pt-Pt distance is conserved across all of these calculations, indicating that the trend is not an artifact of the particular choice of functional. The energetic difference between the low lying excited states, $\Delta \mathrm{E}(\mathrm{S}_2 - \mathrm{S}_1)$, is strongly correlated with the Pt–Pt distance. This splitting is due to the coupling V_c between ϕ_{left} and ϕ_{right}. The results suggest that the coupling (V_c in Eq. (4.6)) between ϕ_{left} and ϕ_{right} increases as the Pt–Pt distance decreases – chemical bonding well-understood from the interaction of frontier orbitals. One can estimate the strength of the coupling V_c between ϕ_{left} and ϕ_{right} by $V_c \approx \frac{1}{2}\Delta \mathrm{E}(\mathrm{S}_2 - \mathrm{S}_1)$ (see Tab. 4.2).

The NTOs for the $S_0 \rightarrow S_1$ and $S_0 \rightarrow S_2$ transitions in Fig. 4.4 explicitly account for the coupling among ϕ_{left}, ϕ_{right} and ϕ_B, and therefore can be used to qualitatively understand the relative coupling strengths in these different molecular complexes. The NTOs for the S_1 and S_2 excited states are more localized on either side of the system for **1** and **2** than those of the structures with shorter Pt–Pt bond lengths (**3** and **4**) where transition densities are delocalized uniformly across both halves of the system. This observation is in agreement with the energetic analysis in which the coupling between ϕ_{left} and ϕ_{right} increases from **1** to **4**. Despite obvious differences in the electron distribution in the S_1 and S_2 states across the four different complexes, the S_1–S_2 splitting can always be understood as arising from the coupling of the diabatic, charge localized orbitals, ϕ_{left} and ϕ_{right}.

Table 4.2 demonstrates the relationship between the Pt–Pt distance and the splitting in the S_1 and S_2 levels of complexes **1–4**. For complexes exhibiting longer Pt–Pt distances (**1** and **2**), the coupling between ϕ_{left} and ϕ_{right} is much weaker than for those with shorter

Pt–Pt distances (**3** and **4**). In such a scenario, even mild interference with the bath states will quickly quench any coherence between ϕ_{left} and ϕ_{right}. As the Pt–Pt distance decreases, the coupling V_c between ϕ_{left} and ϕ_{right} increases significantly, however coupling to the bath may also be affected. If $V_c \gg V_B$, the two–state coherence can persist in the full electronic manifold for many periods of the coherent oscillation. If the opposite is true, strong coupling to bath–type states will result in ultrafast decoherence of the S_1/S_2 wavepacket. Owing to the experimentally observed[3] signatures of a coherent, recurrent exciton transfer in complex **3**, we suspect this complex to exhibit a relatively high ratio of V_c/V_B, and for a wavepacket comprised of S_1 and S_2 to maintain its strict phase relationship for a significant portion of the *ab initio* electronic dynamics simulation. In order to test these hypothesis motivated from the vantage of an effective three state Hamiltonian (Eq. (4.6)), we resort to performing quantum electronic dynamics simulations to directly probe the temporal evolution of a coherent, two state superposition within a realistic, many electron dynamics framework. To support the complex result from the quantum electronic dynamic simulation, we return to the effective three-state model for the dephasing introduced in Eq. (4.6) by resolving approximate diabatic coupling strength ratios between S_1/S_2 and the bath states.

RT-TDDFT Quantum Electronic Dynamic Simulations

The first two excited singlet states for all complexes studied here exhibit substantial charge transfer character, modulated by the different interaction strengths between the two halves of the complex. LR-TDDFT calculations suggest that these excitations are dominated by transitions from the $d\sigma^*$ HOMO to the LUMO (S_1) and LUMO+1 Pt+π^* (S_2) orbitals (Fig. 4.4). The LUMO and LUMO+1 are bonding and antibonding across the Pt–Pt bond. The in-phase and out-of-phase combinations of these two frontier orbitals give rise to a diabatic representation in terms of orbitals localized on either side of the system, $|\phi_{left/right}\rangle = \frac{1}{\sqrt{2}}(|\phi_{LUMO}\rangle \pm |\phi_{LUMO+1}\rangle)$.

To simulate coherent processes following a broadband photoexcitation, the initial condition is prepared by an instantaneous promotion of an electron from the HOMO to LUMO+1 which corresponds to the dominant transition in the $S_0 \rightarrow S_2$ excitation resolved via LR-TDDFT. This procedure creates a wave function that is a superposition of diabatic states with equal contributions from ϕ_{left} and ϕ_{right}. If the system can support coherent electron transfer between ϕ_{left} and ϕ_{right}, one would see anti-correlated population changes in these diabatic orbitals in time. These oscillations should persist for an appreciable length of time if no strong decoherence mechanisms exist. Figure 4.5 plots the time-dependent populations of the localized orbitals, $n_{left}(t)$ and $n_{right}(t)$, following the HOMO→ LUMO+1 excitation. Orbital occupation numbers were determined by projecting the time-dependent density onto localized orbitals, ϕ_{left} and ϕ_{right}, using Eq. (4.5). At longer times the neglect of nuclear motion is a less well founded approximation,[163] so simulations were not continued beyond 50 fs.

For all complexes investigated here, the dynamics begin with both ϕ_{left} and ϕ_{right} half populated, and the changes in their populations evolve in an anti-correlated fashion in the first 10 fs. From Fig. 4.5, it is clear that in complexes **1** and **2** the coherent population oscillation between ϕ_{left} and ϕ_{right} quickly collapses after the first period. While the populations of the localized orbitals do appear to be anti-correlated to some degree in the earliest moments of the simulation, analysis shows that there is a fast relaxation and repopulation of the HOMO, destroying any coherent electronic motion in complexes **1** and **2**. In other words, interaction with the bath states destroys the coherence between ϕ_{left} and ϕ_{right} diabats. Fourier transformation of the orbital occupation time evolution (Fig. 4.6) gives peaks at the energy gaps between each of the eigenstates accessed during the electronic dynamics. Peaks with the greatest intensities in these spectra correspond to the S_1-S_2 energy gap, while the other peaks originate from transitions involving bath-type states. Broad spectra with noisy appearances are resolved for both **1** and **2** over the relevant energy range, suggesting a stronger influence from bath-type states in their electronic dynamics. In contrast, electronic coherence in **3** and **4** is sustained for the whole simulation time, oscillating at a nearly constant frequency $\omega \approx \Delta E(S_2 - S_1)$, as indicated by the cleaner spectra of **3** and **4**. The principle Fourier mode in Fig. 4.6 occurs at approximately the S_1-S_2 energy gap, and lower-frequency peaks are due to resonances between higher-lying excited states which contribute slightly to the electronic wave packet formed by the single orbital swap.

The coherent, recurrent electronic motions along the Pt–Pt bonding direction can also be analyzed in terms of physically observable quantities, such as the time-dependent dipole moment (Eq. (4.4)). Figure 4.7 plots the time-dependent dipole moment along the Pt–Pt bond. A similar observation and conclusion can be made from Fig. 4.5. The electronic coherence can be clearly observed in complexes **3** and **4**, but is not sustainable in complexes **1** or **2**. This suggests that long-lived coherence between low-lying valence states may not be ubiquitous in these types of complexes, but rather that complexes **3-4** exemplify the situation where the coherent subsystem is effectively decoupled from bath-type states, allowing for persistent, recurrent electron transfer between ppy ligands.

From inspection of the electronic density evolution expressed in the basis of the canonical molecular orbitals, Fig. 4.8, it is clear that the loss of coherence in the S_1–S_2 subsystem is accompanied by a concomitant rise in the contribution to the electronic wavepacket from the HOMO. Such population dynamics are indicative of interactions with the electronic ground state, S_0, dominating the dephasing mechanism. In this case, the set of bath states in Eq. (4.6) can, to a good approximation, be represented by S_0. The assignment of S_0 as the dominant bath state is consistent with the HOMO of these systems being substantially delocalized across both ppy ligands, metal centers, and (to some extent) the pyrazolate bridging ligands (see Fig. 4.4 for HOMO isosurfaces).

The ratio of the diabatic coupling strength between S_1 and S_2 to that between S_1/S_2 and the ground state is a renormalized measure of the strength of the two-level subsystem coherence exhibited by **1-4**. A commonly-applied approach to resolving the approximate diabatic coupling strength between two states defined strictly in terms of matrix elements of the Hamiltonian and dipole operators evaluated in the adiabatic basis, namely the Mulliken-Hush theory,[164–166] was invoked in order to approximately resolve V_B. The off-diagonal elements of the electronic Hamiltonian between pairs of donating and accepting charge-localized states, H_{da}, were evaluated for the S_0–S_1 and S_0–S_2 donor-acceptor pairs according to Eq. (4.9).

$$H_{da} = \frac{\mu_{ij}\left(E_i - E_j\right)}{\sqrt{\left(\mu_{ii} - \mu_{jj}\right)^2 + 4\mu_{ij}^2}} \tag{4.9}$$

The mean diabatic coupling strengths between S_1/S_2 and S_0 are equated to V_B, and are presented in Tab. 4.2 as ratios of the relevant coupling strengths, ${}^{V_c}/{}_{V_B}$. Interpreted in light of the so-called golden rule of time-dependent perturbation theory, the square of this ratio is proportional to the rate at which population is lost from the two-level coherence to the bath. So, the order of magnitude difference in the ratios, ${}^{V_c}/{}_{V_B}$, observed for **1-2** and **3-4** are indicative of a $\sim$100× increase in the electronic dephasing timescale for **3-4** relative to **1-2**. This analysis lends support to the results from our mean-field, many-electronic dynamics simulations of the two-level subsystem coherence, and suggests that experimental observation of electronic coherence between the low-lying charge transfer states in binuclear complexes exhibiting longer Pt-Pt distances will challenge the time-resolution attainable even with modern light sources.

Conclusions and Perspective

Real-time time-dependent density functional theory was employed to track the excited state electronic coherence in several binuclear platinum (II) complexes. The ability to support coherent electronic motion and the period of the charge density oscillation between the two halves of these complexes are determined by their electronic couplings which are strongly correlated with the Pt–Pt distances and can be tuned through chemical modification of the bridging ligand's steric bulkiness. Systems with short Pt–Pt distances and whose low-lying transitions are characterized as MMLCT support some degree of long-lived, recurrent electron transfer across the plane bisecting the two halves of the system. Systems exhibiting greater Pt–Pt separations seem incapable of sustaining the same type of coherent states due to stronger electronic couplings to states external to the 2-state subsystem. Evidence for the long-lived electronic coherence is provided in the form of populations of orbitals localized on either side of the system and in the oscillations of the time-dependent dipole. The period of the charge oscillations across the two halves of the system is much shorter than that observed in the early-time response (i.e. prior to spin crossover transition) in the pump-probe experiments.[3] This suggests that the experimentally observed oscillation in the transient absorption anisotropy is the result of coherent electronic and nuclear motions. The evolving electronic superposition (which determines the forces on the nuclei) and the nuclear evolution (which modulates the energies of the states in the electronic superposition) contribute non-separably to the full molecular evolution, so the experimentally resolved signal cannot be completely reproduced by a static-splitting model.

To begin to unravel the role of nuclear motions in the experimentally observed spin crossover and long-lived triplet coherence, the potential energy surfaces of the relevant excited states were resolved along the interplatinum distance coordinate with 0.05 Å resolution at the same level of theory used throughout this work, where all remaining vibrational degrees of freedom were optimized to their minimum energy configurations. These potential energy surfaces were resolved with both the S_1 and S_2 states contributing the forces during the constrained optimizations, and the resulting surfaces are shown plotted in Fig. 4.9. Since the vibrational modes involving interplatinum stretching motions are associated with long periods relative to the other normal modes of vibration (owing to the high reduced mass associated to these modes) these constrained optimization scans can be considered representative one-dimensional potential energy surfaces for the excited state spin crossover reaction coordinate.

The highly-crossed nature of the S_1 and triplet surfaces is revealed in these reduced dimensional potential energy surfaces, which is exactly the scenario needed to support the experimentally observed vibrationally driven spin crossover transition in the excited state dynamics. The so-called "Energy Gap Law" of Jortner and coworkers,[167] which relies on a perturbative treatment of the non-radiative transition rate between electronic states of different spin multiplicity, gives the transition probability as an exponential function of the energy gap. Therefore, much of the complicated spin dynamics implicated in the excited state spin crossover can be understood in terms of motions along the excited state reaction coordinate that bring singlet and triplet states into degeneracy (or nearly so). Clearly, excitation to a superposition of S_1 and S_2 results in forces on the nuclei that favor the contraction of the Pt-Pt distance, where the S_1 curve then quickly crosses a pair of triplet states at approximately 2.85 Å. It is posited here that these are most likely the states accessed immediately through the spin crossover transition.

At this point along the interplatinum distance coordinate, analogous constrained optimizations can be performed subject to the forces of the states populated following the spin crossover (Fig. 4.10). For this preliminary work, it is assumed that the lower-lying of the two triplet states that crosses the S_1 curve will dominate the superposition in the triplet manifold, though a comparison of the magnitude of the coupling strengths between the states is required to rigorously support this assumption. At the configuration associated with the crossing point in the singlet and triplet surfaces, this triplet state contributes nuclear forces that favor elongation of the Pt-Pt distance. Interestingly, the two lowest lying triplet states at $\sim$ 2.9 Å and longer interplatinum distances are split by only a few hundredths of an eV, and this splitting is relatively constant over a large range of Pt-Pt distances surrounding the shallow minimum centered at $\sim$ 3.0Å. Fascinatingly, the splitting in these triplet states is consistent with the timescale in the periodic beating in the anisotropy of the transient absorption signal observed in experiment. From this vantage, it seems very likely that the impulsive photoexcitation of the system to a (superposition of) singlet charge transfer state(s) is responsible for setting up the vibrational wavepacket motion that both facilitates the spin crossover, and drives the system toward a shallow local minimum on the triplet surfaces centered at longer Pt-Pt lengths that facilitates the long-lived two state triplet coherence observed in the transient absorption anisotropy. Future work in this area will utilize relativistic quantum chemical methods for treating the non-adiabatic coupling strength between the singlet and triplet states to confirm the viability of the excited state intersystem crossing and internal conversion pathways suggested by the excited state potential energy surfaces presented here.

Supporting Information: Linear Reponse TDDFT Results with Different Exchange-Correlation Functionals

Table 4.3: S_1-S_2 energy gap (eV) from LR-TDDFT using various exchange-correlation functionals, mixes of exact (Hartree-Fock) exchange and semi-local DFT exchange, and range separation cutoffs for the range-separated hybrids.

	B3LYP	PBE0	B3PW91	LC-ωPBE
1	0.078	0.0847	0.0800	0.0891
2	0.1337	0.1432	0.1399	0.103
3	0.2047	0.2139	0.2029	0.2847
4	0.2583	0.2703	0.2556	0.3828

Supporting Information: Crystal Structure geometries for 1-4

Presented below are the coordinates (in Å) extracted from X-ray crystallography results for each of the studied complexes.

[(ppy)Pt(μ-pz)]$_2$

C	1.944683	2.842746	0.489229
C	2.407732	3.802153	1.374152
C	3.323527	3.453798	2.345023
C	3.762670	2.137134	2.419803
C	3.263968	1.190183	1.522441
C	3.561607	-0.244030	1.551228
C	4.490536	-0.820641	2.411362
C	4.713116	-2.189565	2.378428
C	3.995081	-2.967579	1.506644
C	3.049228	-2.392036	0.648365
C	2.824314	-1.023044	0.637968

C	-2.105026	-2.701271	1.015382
C	-2.735154	-3.493403	1.962075
C	-3.712808	-2.929935	2.758058
C	-4.009607	-1.598914	2.617179
C	-3.341375	-0.815907	1.674329
C	-3.503059	0.624504	1.477675
C	-4.349988	1.420988	2.240910
C	-4.374499	2.787533	2.042431
C	-3.573848	3.347022	1.060411
C	-2.758984	2.551584	0.269941
C	-2.695775	1.170462	0.442750
C	1.310927	-2.581935	-2.232117
C	0.279908	-3.358224	-2.690077
C	-0.870761	-2.742102	-2.240493
C	0.827844	2.190019	-2.778591
C	-0.317647	2.626324	-3.413420
C	-1.338183	1.927463	-2.805996
H	2.553262	-2.951356	0.061549
H	-1.429162	-3.086187	0.467960
H	-2.498108	-4.408328	2.062611
H	-4.175987	-3.460379	3.396458
H	-4.675190	-1.204529	3.167363
H	-4.911085	1.025491	2.899242
H	-4.935188	3.338576	2.574568
H	1.320265	3.091000	-0.181869
H	-3.584257	4.288518	0.926966
H	-2.230553	2.957988	-0.406277
H	2.233981	-2.754884	-2.382528

H	0.344561	-4.151907	-3.207105
H	-1.756997	-3.048394	-2.394940
H	1.708097	2.488556	-2.974693
H	-0.386662	3.268453	-4.111354
H	-2.257146	2.005453	-3.031809
H	2.095175	4.698756	1.312686
H	3.651116	4.106261	2.955499
H	4.396516	1.880250	3.078148
H	4.972646	-0.277741	3.022415
H	5.357786	-2.583651	2.954138
H	4.140984	-3.904666	1.484775
N	2.365491	1.551374	0.564390
N	-2.421127	-1.399941	0.845748
N	0.826211	-1.538034	-1.543106
N	-0.537012	-1.639290	-1.549070
N	0.509752	1.267481	-1.833212
N	-0.853047	1.121736	-1.857686
Pt	1.632878	0.044968	-0.562084
Pt	-1.627448	-0.174974	-0.542709

[(ppy)Pt(μ-Me$_2$pz)]$_2$

C	-2.237116	-2.680887	0.886887
C	-2.887386	-3.558047	1.781735
C	-3.740300	-3.049760	2.660411
C	-3.987073	-1.666990	2.720334
C	-3.329438	-0.860428	1.811531
C	-3.421020	0.584619	1.730251
C	-4.284309	1.326478	2.576392
C	-4.253032	2.715840	2.473411
C	-3.411244	3.372350	1.613099
C	-2.575399	2.629384	0.765670
C	-2.594102	1.226943	0.787461
C	2.246274	2.725701	0.846776
C	2.751958	3.624775	1.774655
C	3.463435	3.096731	2.856724
C	3.680722	1.781186	2.986837
C	3.137852	0.908795	1.983596
C	3.245783	-0.561195	1.972461
C	3.904229	-1.270246	2.992192
C	3.931351	-2.638318	2.891599
C	3.342593	-3.326535	1.805579
C	2.671463	-2.567333	0.823545
C	2.615154	-1.209295	0.874504
C	-1.244341	2.223804	-2.429390
C	-0.192215	2.862182	-3.044526
C	0.966423	2.332304	-2.454237
C	-0.868398	-2.429744	-2.375437

C	0.278723	-2.908378	-2.965847
C	1.340208	-2.233431	-2.428251
C	-2.710026	2.333557	-2.681578
C	2.423244	2.587589	-2.819255
C	2.822891	-2.327376	-2.679167
C	-2.290561	-2.798209	-2.662479
H	-2.002120	3.071201	0.183620
H	1.766141	3.056153	0.121896
H	2.623516	4.541110	1.680133
H	3.794017	3.675464	3.505090
H	4.167237	1.443028	3.703477
H	4.305958	-0.829637	3.706147
H	4.352187	-3.130431	3.560806
H	-1.645243	-3.038471	0.265111
H	3.396041	-4.253092	1.739672
H	2.253160	-3.009778	0.119586
H	-0.237222	3.509126	-3.711610
H	0.324757	-3.571936	-3.616974
H	-3.181381	1.734797	-2.095903
H	-2.997025	3.235256	-2.514087
H	-2.897388	2.102238	-3.593194
H	-2.721117	-4.472815	1.755296
H	2.992893	2.100555	-2.221096
H	2.581500	2.297318	-3.721157
H	2.610105	3.526878	-2.747818
H	3.279523	-1.662918	-2.155094
H	3.135716	-3.200338	-2.430932
H	3.000617	-2.176382	-3.609716

H	-2.873814	-2.295278	-2.091555
H	-2.492810	-2.599918	-3.579617
H	-2.416353	-3.736391	-2.503415
H	-4.184130	-3.617534	3.247894
H	-4.572112	-1.308175	3.349166
H	-4.849144	0.902289	3.180780
H	-4.826329	3.216361	3.008182
H	-3.393178	4.302413	1.593249
N	-2.430419	-1.381423	0.896224
N	2.422102	1.401127	0.950307
N	-0.752849	1.346666	-1.506059
N	0.618209	1.421682	-1.568903
N	-0.520629	-1.498383	-1.514386
N	0.859060	-1.383470	-1.526785
Pt	-1.571282	-0.056065	-0.349703
Pt	1.655380	0.047977	-0.351498

$[(ppy)Pt(\mu\text{-}{}^tBu_2pz)]_2$

C	2.202903	0.257467	-2.031529
C	2.083588	1.465700	-2.669298
C	2.632999	1.679496	-3.925554
C	3.282786	0.646892	-4.571294
C	3.383913	-0.580474	-3.955665
C	2.844218	-0.760724	-2.674724
C	2.877378	-2.024414	-1.926425
C	2.094346	-3.139365	0.020559
C	2.672421	-4.315181	-0.421456
C	3.378820	-4.336232	-1.615259
C	3.471937	-3.184539	-2.370202
C	-1.046080	-1.103932	2.876709
C	0.067859	-1.354991	3.654342
C	1.179072	-1.083859	2.861455
C	2.607121	-0.919389	3.365720
C	3.677308	-1.296847	2.339715
C	2.740891	0.555808	3.744893
C	2.800770	-1.766891	4.629146
C	-2.473139	-1.071336	3.405716
C	-3.558598	-1.072582	2.333358
C	-2.593477	0.218688	4.236696
C	-2.703089	-2.273953	4.320426
C	1.186792	2.992760	0.364158
C	0.088597	3.815140	0.518366
C	-1.036830	3.022809	0.455847
C	-2.442055	3.520720	0.725291

C	-3.521900	2.449200	0.730813
C	-2.811255	4.602085	-0.297709
C	-2.438080	4.179871	2.116941
C	2.637582	3.449945	0.510014
C	2.927322	4.532770	-0.539780
C	2.770543	4.064033	1.915940
C	3.682478	2.343151	0.358056
C	-3.042302	-1.902619	-1.751836
C	-3.709385	-3.064412	-2.135966
C	-3.542241	-4.228891	-1.402892
C	-2.688667	-4.229060	-0.316091
C	-2.055706	-3.052187	0.044285
C	-3.105482	-0.637738	-2.461053
C	-2.333285	0.383960	-1.890403
C	-2.288189	1.608025	-2.538079
C	-3.028012	1.833906	-3.694994
C	-3.796715	0.805514	-4.236939
C	-3.824801	-0.414163	-3.635668
H	1.624167	2.157465	-2.251643
H	2.562183	2.513395	-4.332212
H	3.652631	0.779493	-5.413105
H	3.806511	-1.287132	-4.385619
H	1.625757	-3.139430	0.821960
H	2.586411	-5.091870	0.083711
H	3.788340	-5.120123	-1.905213
H	3.934243	-3.190422	-3.174942
H	0.075088	-1.648002	4.536915
H	0.105781	4.735845	0.641072

H	-4.265125	-3.058953	-2.882484
H	-3.998796	-5.002562	-1.639445
H	-2.541064	-5.008882	0.169600
H	-1.483139	-3.053410	0.777654
H	-1.755995	2.288645	-2.195450
H	-3.009770	2.669011	-4.103953
H	-4.291432	0.953245	-5.011185
H	-4.324007	-1.103155	-4.009276
H	3.598441	-2.228025	2.124427
H	4.545735	-1.125486	2.707389
H	3.557722	-0.772345	1.544578
H	2.573575	1.102566	2.973260
H	3.628185	0.725011	4.068939
H	2.103318	0.770018	4.430756
H	2.233428	-1.434017	5.326676
H	3.717120	-1.717152	4.910375
H	2.574057	-2.680250	4.441962
H	-3.376595	-0.380187	1.693529
H	-4.412130	-0.916950	2.741690
H	-3.566469	-1.923790	1.888191
H	-2.457453	0.980122	3.669700
H	-1.929868	0.214108	4.932633
H	-3.467974	0.264916	4.630188
H	-3.590650	-2.236084	4.682414
H	-2.063321	-2.258556	5.037612
H	-2.598996	-3.085039	3.816852
H	-3.562963	2.032745	-0.134875
H	-4.370464	2.850871	0.933240

H	-3.312917	1.788770	1.395345
H	-2.194973	5.334566	-0.225400
H	-3.702516	4.914584	-0.125335
H	-2.768128	4.233456	-1.181477
H	-2.177798	3.531961	2.775258
H	-3.319143	4.504947	2.320792
H	-1.817428	4.911828	2.123870
H	3.804455	4.893569	-0.394729
H	2.275534	5.233250	-0.465673
H	2.881869	4.145724	-1.419640
H	2.500436	3.419061	2.572671
H	2.208118	4.840807	1.981598
H	3.683409	4.316637	2.070884
H	3.505233	1.646375	0.993741
H	4.556986	2.705570	0.516240
H	3.641623	1.982160	-0.532245
N	2.196167	-1.959514	-0.702994
N	0.741222	-0.720649	1.632680
N	-0.638768	-0.728759	1.650360
N	0.739791	1.735171	0.183683
N	-0.638833	1.748075	0.228740
N	-2.246770	-1.886614	-0.645735
Pt	-1.471576	-0.101640	-0.155551
Pt	1.502666	-0.167306	-0.200510

[(ppy)Pt(μ-Ph$_2$pz)]$_2$

C	-2.193901	1.643108	-1.376019
C	-2.194100	1.496555	-2.753054
C	-2.725365	2.462320	-3.587605
C	-3.275400	3.614640	-3.047357
C	-3.282011	3.796188	-1.686416
C	-2.722659	2.809415	-0.859534
C	-2.645440	2.911987	0.602409
C	-3.061988	4.012370	1.361227
C	-2.932819	3.986899	2.738813
C	-2.401997	2.862044	3.348409
C	-1.992385	1.793660	2.584498
C	2.022812	1.718266	-1.499589
C	2.036256	1.450723	-2.847415
C	2.430884	2.418285	-3.754330
C	2.778236	3.680391	-3.327818
C	2.784700	3.960934	-1.971768
C	2.401147	2.964367	-1.071715
C	2.396428	3.120953	0.385264
C	2.707766	4.300170	1.072412
C	2.604986	4.342741	2.445305
C	2.215798	3.210092	3.137334
C	1.904393	2.042877	2.456181
C	1.242916	-1.648043	2.348060
C	2.686430	-1.889225	2.568764
C	3.090919	-2.873940	3.469871

C	4.418838	-3.081080	3.742236
C	5.384285	-2.324514	3.111986
C	5.025018	-1.365816	2.191409
C	3.668850	-1.147662	1.940716
C	0.160312	-2.241580	2.993898
C	-1.003038	-1.701593	2.417270
C	-2.396273	-2.035224	2.685408
C	-2.692247	-3.034792	3.622471
C	-4.006700	-3.460465	3.821547
C	-5.030241	-2.911567	3.088512
C	-4.760746	-1.898977	2.193142
C	-3.466450	-1.459295	2.007829
C	1.150082	-2.106781	-2.024111
C	0.050636	-2.790775	-2.524506
C	-1.078341	-2.086387	-2.086738
C	-2.486901	-2.443213	-2.312800
C	-2.795474	-3.465527	-3.237996
C	-4.104694	-3.873349	-3.406891
C	-5.133897	-3.290868	-2.689909
C	-4.833912	-2.279567	-1.800810
C	-3.535803	-1.855739	-1.622048
C	2.586133	-2.433121	-2.199485
C	3.603850	-1.562189	-1.894118
C	4.937755	-1.907540	-2.144662
C	5.242701	-3.130813	-2.679699
C	4.238635	-4.021735	-2.954899
C	2.908983	-3.673393	-2.726308
H	-2.322642	2.829401	4.274396

H	-1.639354	1.042763	3.006887
H	1.776599	0.611649	-3.153082
H	2.463270	2.212915	-4.660935
H	3.007448	4.339101	-3.943490
H	3.039347	4.801009	-1.665159
H	2.982327	5.054930	0.602233
H	2.795867	5.127889	2.904212
H	2.162126	3.231475	4.065770
H	1.630753	1.292120	2.933370
H	2.448920	-3.398649	3.892731
H	4.669686	-3.734881	4.355424
H	6.283038	-2.462603	3.310386
H	5.672276	-0.870117	1.745619
H	3.420922	-0.487859	1.334560
H	-1.826935	0.727337	-3.125547
H	0.200374	-2.873315	3.674658
H	-2.003974	-3.416722	4.118569
H	-4.190077	-4.119178	4.451747
H	-5.900587	-3.222361	3.195640
H	-5.452178	-1.510041	1.711005
H	-3.305512	-0.760562	1.416358
H	0.062468	-3.561986	-3.044093
H	-2.714790	2.337948	-4.509494
H	-2.115811	-3.861853	-3.733056
H	-4.294877	-4.551556	-4.011843
H	-6.011685	-3.575749	-2.804891
H	-5.518458	-1.878244	-1.315808
H	-3.359501	-1.162533	-1.027262

H	3.404639	-0.736000	-1.515716
H	5.618650	-1.305589	-1.948066
H	-3.638886	4.264485	-3.605834
H	6.126738	-3.357049	-2.855458
H	4.444417	-4.862910	-3.296216
H	2.233144	-4.278347	-2.927846
H	-3.654142	4.562406	-1.316978
H	-3.426042	4.757270	0.940714
H	-3.200561	4.716154	3.248475
N	-2.093536	1.803125	1.205240
N	1.993273	1.977305	1.074137
N	0.709257	-1.022419	-1.328570
N	-0.659479	-1.017174	-1.359307
N	0.764630	-0.772323	1.427148
N	-0.604921	-0.825050	1.466429
Pt	-1.454627	0.370512	-0.023919
Pt	1.452148	0.442946	-0.073539

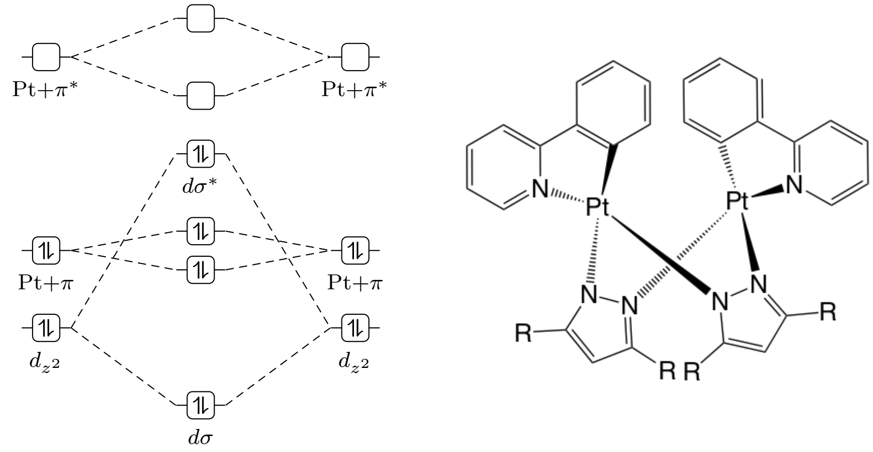

Figure 4.1: Molecular orbital diagram (left) and structure for the pyrazolate bridged, ppy cyclometalated diplatinum complexes (right) with R = H (**1**), Me (**2**), ^{t}Bu (**3**), and Ph (**4**.)Reproduced with permission from reference 168.

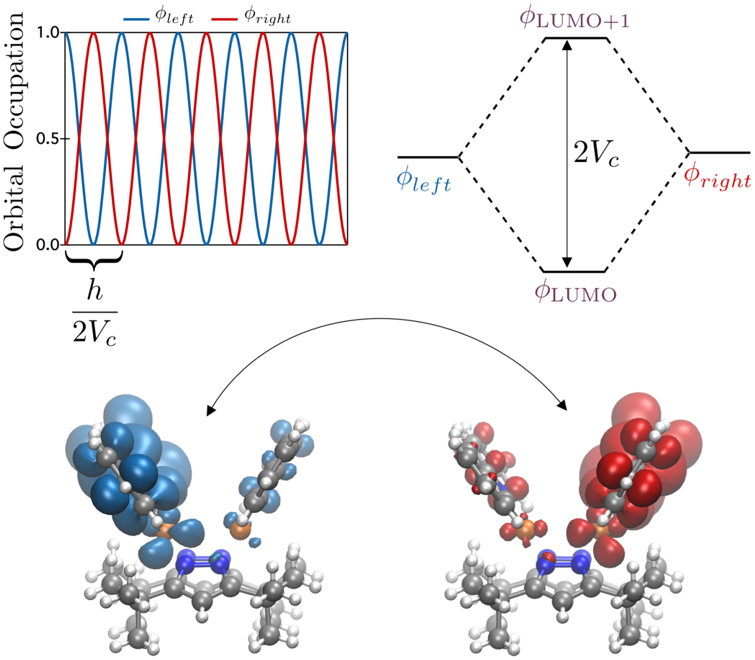

Figure 4.2: Schematic of the theoretical model used to explain the periodic beating in the TA anisotropy in Ref. 3. The in-phase (ϕ_{LUMO}) and out-of-phase ($\phi_{\mathrm{LUMO+1}}$) orbitals are formed from orbitals localized on either side of the system (ϕ_{left} and ϕ_{right}). The coherent electron transfer can be analyzed in terms of the contribution of these localized orbitals to the time evolving density. Reproduced with permission from reference 168.

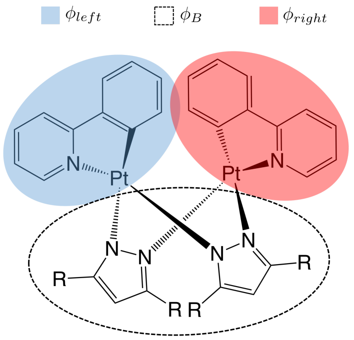

Figure 4.3: Schematic illustration of diabatic electronic wave functions. Reproduced with permission from reference 168.

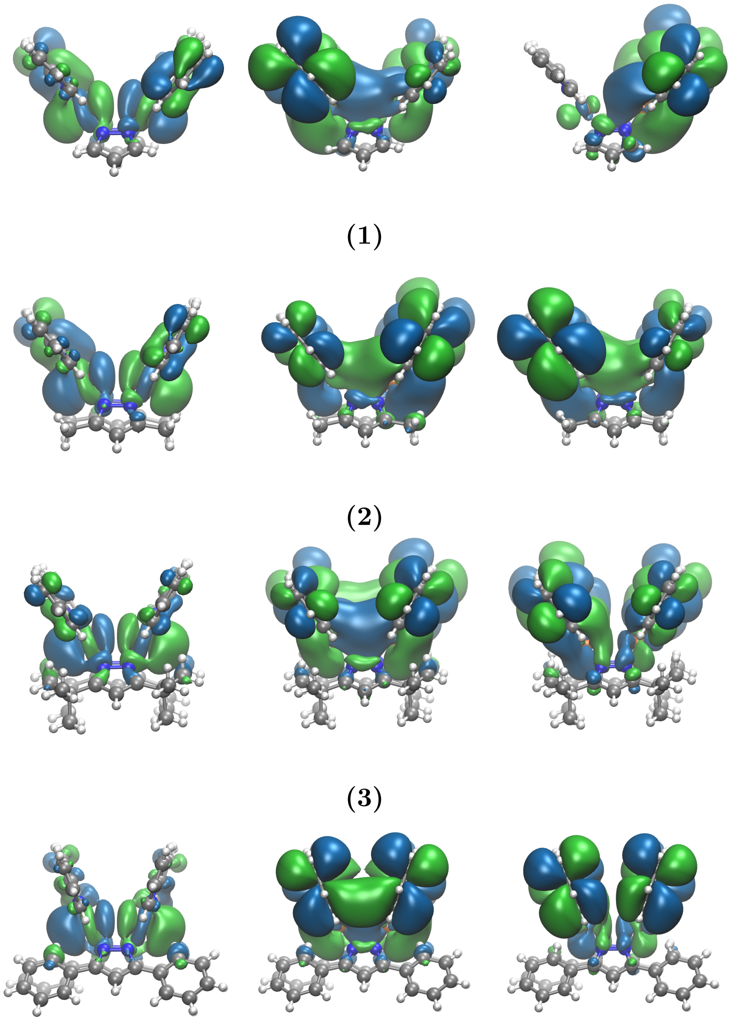

(1)

(2)

(3)

(4)

Figure 4.4: HOMO (left panel), electronic NTO's of the S_1 (middle panel) and S_2 (right panel) states in molecular complexes **1-4** with decreasing Pt–Pt separation distance. Reproduced with permission from reference 168.

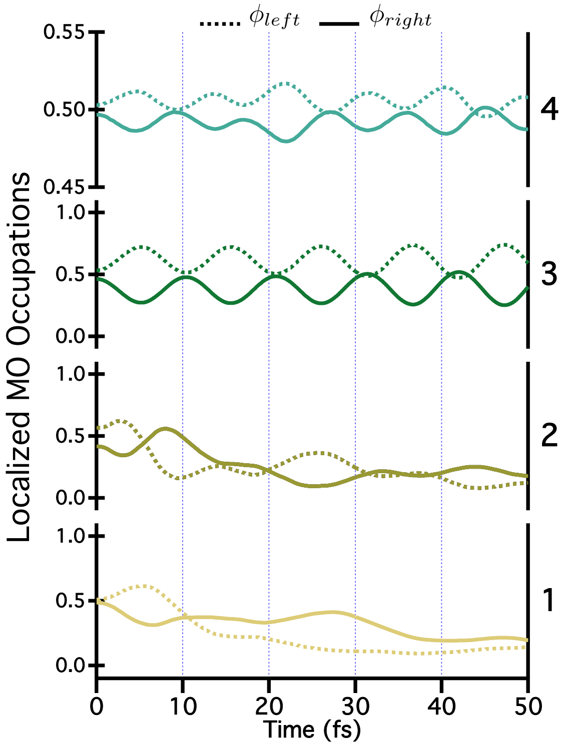

Figure 4.5: Time evolving fractional occupation numbers of the local orbitals ϕ_{left} and ϕ_{right} of complexes **1**–**4** following a HOMO → LUMO+1 excitation (10 fs moving average). Reproduced with permission from reference 168.

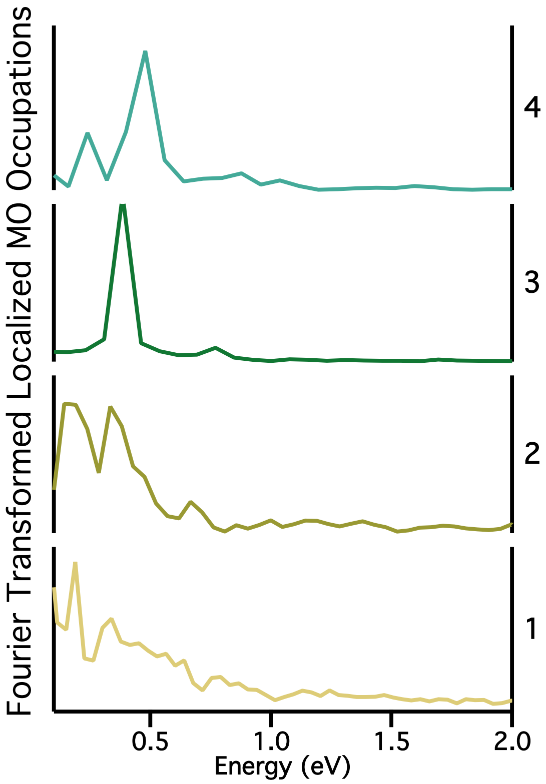

Figure 4.6: Magnitudes of the Fourier transformed fractional occupation numbers for one of the localized orbitals (ϕ_{left}), for **1–4**, following a HOMO → LUMO+1 excitation. Reproduced with permission from reference 168.

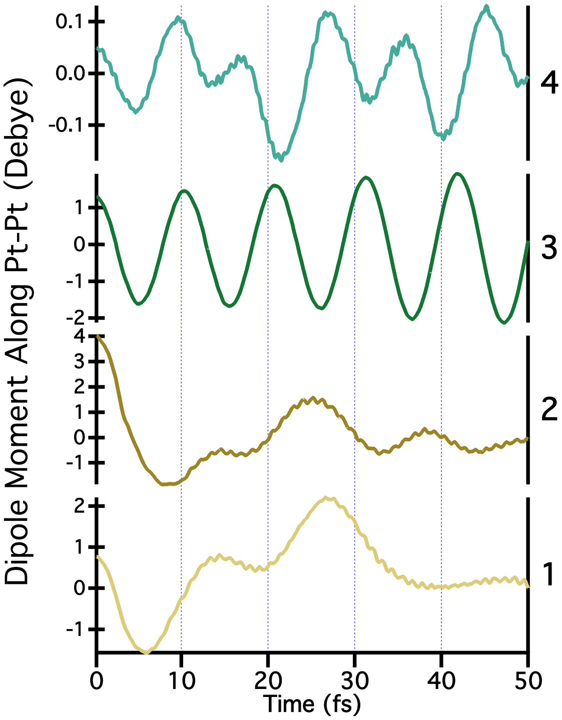

Figure 4.7: Time evolving dipole moments for **1**–**4** collinear with the Pt–Pt bond, following a HOMO → LUMO+1 excitation (10 fs moving average). Reproduced with permission from reference 168.

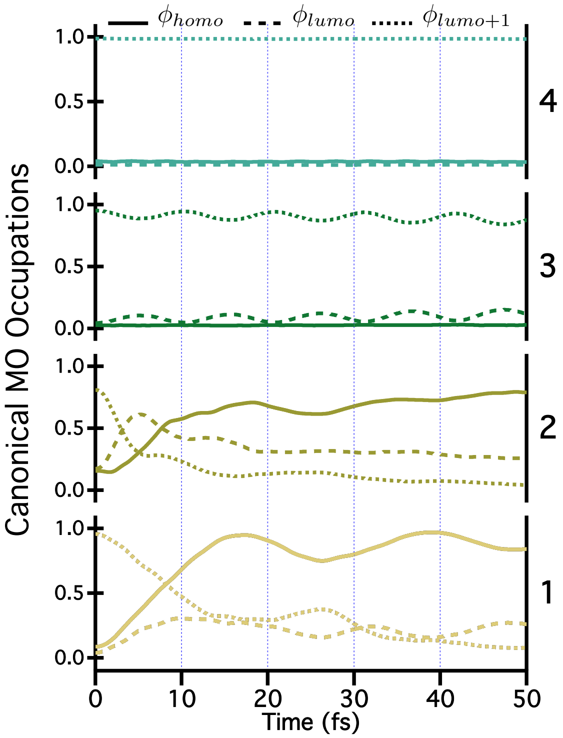

Figure 4.8: Contributions of the canonical molecular orbitals to the time evolving density for **1** − **4** (10fs moving average). Reproduced with permission from reference 168.

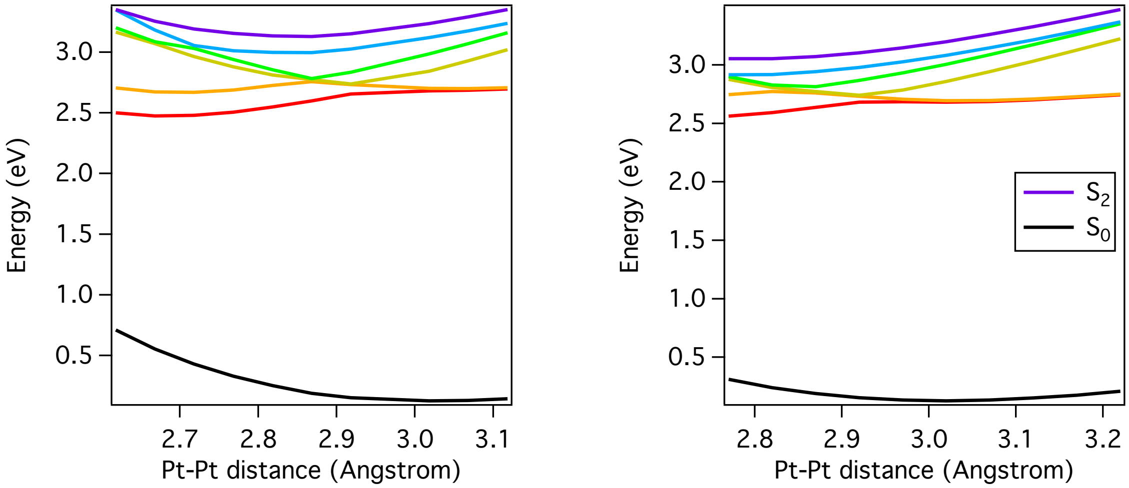

Figure 4.9: Potential energy surface along the Pt-Pt distance, with remaining geometric parameters optimized for each Pt-Pt distance according to forces in the S_1 (Left) and S_2 (Right) state. In both cases, S_1 crosses two nearly-degenerate triplet states at ~ 2.85 Å, and is therefore shown in orange at distances < 2.85 Å and green at longer ones. All surfaces not otherwise identified correspond to triplets. Reproduced with permission from reference 168.

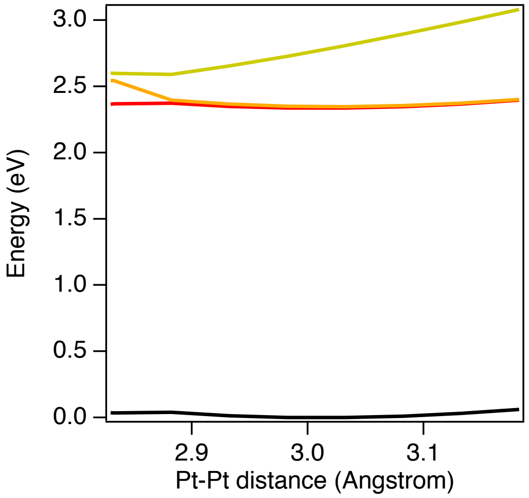

Figure 4.10: Potential energy surface along the Pt-Pt distance, with remaining geometric parameters optimized for each Pt-Pt distance according to forces from the lower-energy triplet state (orange, both here and in Fig. 4.9) that crosses the S_1 surface (yellow) at ∼ 2.85 Å. Reproduced with permission from reference 168.

BIBLIOGRAPHY

[1] Lingerfelt, D. B.; Williams-Young, D. B.; Petrone, A.; Li, X. **2016**, *12*, 935–945.

[2] Goings, J. J.; Lingerfelt, D. B.; Li, X. **2016**, *7*, 5193–5197.

[3] Cho, S.; Mara, M. W.; Wang, X.; Lockard, J. V.; Rachford, A. A.; Castellano, F. N.; Chen, L. X. *J. Phys. Chem. A* **2011**, *115*, 3990–3996.

[4] Marx, D.; Hutter, J. *Ab Initio Molecular Dynamics: Basic Theory and Advanced Methods*; Cambridge University Press, 2009.

[5] Lorenz, C.; Doltsinis, N. In *Handbook of Computational Chemistry*; Leszczynski, J., Ed.; Springer Netherlands, 2014; pp 195–238.

[6] Frenkel, D.; Smit, B. *Understanding Molecular Simulation: From Algorithms to Applications*; Computational Science Series; Elsevier Science, 2001.

[7] Lingerfelt, D. B.; Fischer, S. A.; May, J. W.; Li, X. **2014**, *118*, 3266–3273.

[8] Heller, E. J. *Acc. Chem. Res.* **1981**, *14*, 368–375.

[9] Barbatti, M.; Aquino, A. J. A.; Lischka, H. *Phys. Chem. Chem. Phys.* **2010**, *12*, 4959–4967.

[10] Petit, A. S.; Subotnik, J. E. *J. Chem. Phys.* **2014**, *141*, 154108.

[11] Mikosch, J.; Trippel, S.; Eichhorn, C.; Otto, R.; Lourderaj, U.; Zhang, J. X.; Hase, W. L.; Weidemüller, M.; Wester, R. *Science* **2008**, *319*, 183–186.

[12] Marrink, S. J.; Mark, A. E. *J. Am. Chem. Soc.* **2003**, *125*, 11144–11145.

[13] Xie, W.; Bai, S.; Zhu, L.; Shi, Q. *J. Phys. Chem. A* **2013**, *117*, 6196–6204.

[14] Hammes-Schiffer, S.; Tully, J. C. *J. Chem. Phys.* **1994**, *101*, 4657–4667.

[15] Kosloff, R. *J. Phys. Chem.* **1988**, *92*, 2087–2100.

[16] Light, J. C.; Carrington, T. *Advances in Chemical Physics*; John Wiley and Sons, Inc., 2007; pp 263–310.

[17] Meyer, H.-D.; Manthe, U.; Cederbaum, L. *Chem. Phys. Lett.* **1990**, *165*, 73–78.

[18] C. Tully, J. *Faraday Discuss.* **1998**, *110*, 407–419.

[19] Kapral, R.; Ciccotti, G. *J. Chem. Phys.* **1999**, *110*, 8919–8929.

[20] Deumens, E.; Diz, A.; Longo, R.; Öhrn, Y. *Rev. Mod. Phys.* **1994**, *66*, 917–983.

[21] Bastida, A.; Cruz, C.; Zúñiga, J.; Requena, A.; Miguel, B. *Chem. Phys. Lett.* **2006**, *417*, 53–57.

[22] Born, M.; Oppenheimer, R. *Annalen der Physik* **1927**, *389*, 457–484.

[23] Kutzelnigg, W. *Mol. Phys.* **2007**, *105*, 2627–2647.

[24] Massey, H. S. W. *Rep. Prog. Phys.* **1949**, *12*, 248.

[25] Morrissey, B. W. *J. Chem. Educ.* **1975**, *52*, 296–298.

[26] Parandekar, P. V.; Tully, J. C. *J. Chem. Phys.* **2005**, *122*, 094102.

[27] Parandekar, P. V.; Tully, J. C. *J. Chem. Theor. Comput.* **2006**, *2*, 229–235.

[28] Horsfield, A. P.; Bowler, D.; Fisher, A.; Todorov, T. N.; Sánchez, C. G. *J. Phys.–Condens. Mat.* **2004**, *16*, 8251.

[29] Kelly, A.; Brackbill, N.; Markland, T. E. *J. Chem. Phys.* **2015**, *142*, 094110.

[30] Martinez, T. J.; Ben-Nun, M.; Levine, R. D. *J. Phys. Chem.* **1996**, *100*, 7884–7895.

[31] Craig, I. R.; Manolopoulos, D. E. *J. Chem. Phys.* **2004**, *121*, 3368–3373.

[32] Richardson, J. O.; Thoss, M. *J. Chem. Phys.* **2013**, *139*, 031102.

[33] Cao, J.; Voth, G. A. *J. Chem. Phys.* **1994**, *100*, 5106–5117.

[34] Hack, M. D.; Wensmann, A. M.; Truhlar, D. G.; Ben-Nun, M.; Martinez, T. J. *J. Chem. Phys.* **2001**, *115*, 1172–1186.

[35] Worth, G. A.; Hunt, P.; Robb, M. A. *J. Phys. Chem. A* **2003**, *107*, 621–631.

[36] Barbatti, M. *WIRES Comput. Mol. Sci.* **2011**, *1*, 620–633.

[37] Bjerre, A.; Nikitin, E. *Chem. Phys. Lett.* **1967**, *1*, 179–181.

[38] Tully, J. C.; Preston, R. K. *J. Chem. Phys.* **1971**, *55*, 562–572.

[39] Craig, C. F.; Duncan, W. R.; Prezhdo, O. V. *Phys. Rev. Lett.* **2005**, *95*, 163001.

[40] Tapavicza, E.; Tavernelli, I.; Rothlisberger, U. *Phys. Rev. Lett.* **2007**, *98*, 023001.

[41] Plasser, F.; Crespo-Otero, R.; Pederzoli, M.; Pittner, J.; Lischka, H.; Barbatti, M. *J. Chem. Theor. Comput.* **2014**, *10*, 1395–1405.

[42] Du, L.; Lan, Z. *J. Chem. Theor. Comput.* **2015**, *11*, 1360–1374.

[43] Akimov, A. V.; Prezhdo, O. V. *J. Chem. Theor. Comput.* **2013**, *9*, 4959–4972.

[44] Barbatti, M.; Ruckenbauer, M.; Plasser, F.; Pittner, J.; Granucci, G.; Persico, M.; Lischka, H. *WIRES Comput. Mol. Sci.* **2014**, *4*, 26–33.

[45] Richter, M.; Marquetand, P.; Gonzalez-Vazquez, J.; Sola, I.; Gonzalez, L. *J. Chem. Theor. Comput.* **2011**, *7*, 1253–1258.

[46] Zheng, J.; Li, Z.-H.; Jasper, A. W.; Bonhommeau, D. A.; Valero, R.; Meana-Pañeda, R.; Truhlar, D. G. ANT. version 2015. http://comp.chem.umn.edu/ant, 2015.

[47] Alguire, E. C.; Ou, Q.; Subotnik, J. E. *J. Phys. Chem. B* **2015**, *119*, 7140–7149.

[48] Ou, Q.; Alguire, E. C.; Subotnik, J. E. *J. Phys. Chem. B* **2015**, *119*, 7150–7161.

[49] Fatehi, S.; Alguire, E.; Shao, Y.; Subotnik, J. E. *J. Chem. Phys.* **2011**, *135*, 234105.

[50] Send, R.; Furche, F. *J. Chem. Phys.* **2010**, *132*, 044107.

[51] Zhang, X.; Herbert, J. M. *J. Chem. Phys.* **2015**, *142*, 064109.

[52] Li, Z.; Suo, B.; Liu, W. *J. Chem. Phys.* **2014**, *141*, 244105.

[53] Handy, N. C.; Lee, A. M. *Chem. Phys. Lett.* **1996**, *252*, 425–430.

[54] Ben-Nun, M.; Levine, R. *Chem. Phys.* **1995**, *201*, 163–187.

[55] Feng, W.; Xu, L.; Li, X.-Q.; Fang, W.; Yan, Y. *AIP Adv.* **2014**, *4*, 077131.

[56] Martens, C. C.; Fang, J.-Y. *J. Chem. Phys.* **1997**, *106*, 4918–4930.

[57] Burant, J. C.; Tully, J. C. *J. Chem. Phys.* **2000**, *112*, 6097–6103.

[58] Cheng, S. C.; Zhu, C.; Liang, K. K.; Lin, S. H.; Truhlar, D. G. *J. Chem. Phys.* **2008**, *129*, 024112.

[59] Shenvi, N.; Subotnik, J. E.; Yang, W. *J. Chem. Phys.* **2011**, *134*, 144102.

[60] Krishna, V. *J. Chem. Phys.* **2007**, *126*, 134107.

[61] Tully, J. C. *J. Chem. Phys.* **1990**, *93*, 1061–1071.

[62] Jasper, A. W.; Stechmann, S. N.; Truhlar, D. G. *J. Chem. Phys.* **2002**, *116*, 5424–5431.

[63] Runge, E.; Gross, E. K. U. *Phys. Rev. Lett.* **1984**, *52*, 997–1000.

[64] Xu, B. X.; Rajagopal, A. K. *Phys. Rev. A* **1985**, *31*, 2682.

[65] Dhara, A. K.; Ghosh, S. K. *Phys. Rev. A* **1987**, *35*, 442.

[66] Chen, G. H.; Mukamel, S. *J. Chem. Phys.* **1995**, *103*, 9355.

[67] Casida, M. E. *Recent Developments and Applications in Density Functional Theory*; Elsevier: Amsterdam, 1996.

[68] Yabana, K.; Bertsch, G. F. *Phys. Rev. B* **1996**, *54*, 4484.

[69] Marques, M. A. L.; Gross, E. K. U. *Annu. Rev. Phys. Chem.* **2004**, *55*, 427.

[70] Burke, K.; Werschnik, J.; Gross, E. K. U. *J. Chem. Phys.* **2005**, *123*, 062206.

[71] Kulander, K. C. *Phys. Rev. A* **1987**, *36*, 2726.

[72] Kulander, K. C. *Phys. Rev. A* **1987**, *35*, 445.

[73] Field, M. J. *J. Chem. Phys.* **1992**, *96*, 4583.

[74] Liang, W.; Fischer, S. A.; Frisch, M. J.; Li, X. **2011**, *7*, 3540–3547.

[75] Frisch, M. J. et al. Gaussian Development Version Revision H.21. Gaussian Inc., Wallingford CT 2012.

[76] Millam, J. M.; Bakken, V.; Chen, W.; Hase, W. L.; Schlegel, H. B. *J. Chem. Phys.* **1999**, *111*, 3800–3805.

[77] Li, X.; Millam, J. M.; Schlegel, H. B. **2001**, *114*, 8897–8904.

[78] Li, X.; Smith, S. M.; Markevitch, A. N.; Romanov, D. A.; Levis, R. J.; Schlegel, H. B. **2005**, *7*, 233–239.

[79] Li, X.; Tully, J. C.; Schlegel, H. B.; Frisch, M. J. **2005**, *123*, 084106.

[80] Malhado, J. P.; Bearpark, M. J.; Hynes, J. T. *Front. Chem.* **2014**, *2*, 97.

[81] Fernandez-Alberti, S.; Roitberg, A. E.; Nelson, T.; Tretiak, S. *J. Chem. Phys.* **2012**, *137*, 014512.

[82] Wang, L.; Prezhdo, O. V. *J. Phys. Chem. Lett.* **2014**, *5*, 713–719.

[83] Laio, A.; Parrinello, M. *Proc. Natl. Acad. Sci. U.S.A.* **2002**, *99*, 12562–12566.

[84] Laio, A.; Gervasio, F. L. *Rep. Prog. Phys.* **2008**, *71*, 126601.

[85] Fischer, S. A.; Chapman, C. T.; Li, X. **2011**, *135*, 144102.

[86] Hammes-Schiffer, S.; Tully, J. C. *J. Chem. Phys.* **1995**, *103*, 8528–8537.

[87] Nangia, S.; Jasper, A. W.; Miller, T. F.; Truhlar, D. G. *J. Chem. Phys.* **2004**, *120*, 3586–3597.

[88] Cohen-Tannoudji, C.; Diu, B.; Laloe, F. *Quantum Mechanics*; Wiley, 1991; pp 1283–1303, v. 1.

[89] Schatz, G.; Ratner, M. *Quantum Mechanics in Chemistry*; Dover Publications, 2012; pp 70–74.

[90] Sauer, S. *Molecular Electromagnetism: A Computational Chemistry Approach*; OUP Oxford, 2011; pp 30–66.

[91] Peslherbe, G. H.; Wang, H.; Hase, W. L. *Advances in Chemical Physics*; John Wiley and Sons, Inc., 2007; pp 171–201.

[92] Hase, W. L.; R. J. Duchovic, X. H.; Komornicki, A.; Lim, K. F.; Lu, D.-H.; Peslherbe, G. H.; Swamy, K. N.; Linde, S. R. V.; Varandas, A.; Wang, H.; Wolf, R. J. *Quant. Chem. Prog. Exch.* **1996**, *16*, 671.

[93] Kilina, S. V.; Kilin, D. S.; Prezhdo, V. V.; Prezhdo, O. V. *J. Phys. Chem. C* **2011**, *115*, 21641–21651.

[94] Dalgarno, A.; Stewart, A. L. *Proc. R. Soc. Lond. A Math Phys. Sci.* **1958**, *247*, 245–259.

[95] Sternheimer, R. M.; Foley, H. M. *Phys. Rev.* **1953**, *92*, 1460–1468.

[96] Yabana, K.; Bertsch, G. F. *Phys. Rev. B* **1996**, *54*, 4484–4487.

[97] Lingerfelt, D. B.; Williams-Young, D. B.; Petrone, A.; Li, X. *J. Chem. Theory Comp.* **2016**, *12*, 935–945, PMID: 26855086.

[98] Frisch, M. J. et al. Gaussian Development Version Revision I.04+. Gaussian Inc., Wallingford CT 2016.

[99] Franck, J.; Dymond, E. G. *Trans. Faraday Soc.* **1926**, *21*, 536–542.

[100] Condon, E. *Phys. Rev.* **1926**, *28*, 1182–1201.

[101] Sponer, H.; Teller, E. *Rev. Mod. Phys.* **1941**, *13*, 75–170.

[102] Barone, V. **2016**, *6*, 86–110.

[103] Egidi, F.; Bloino, J.; Cappelli, C.; Barone, V. *J. Chem. Theor. Comput.* **2014**, *10*, 346–363.

[104] Condon, E. U. *Phys. Rev.* **1928**, *32*, 858–872.

[105] Gorokhov, A. V. *Sov. Phys. Jour.* **1971**, *14*, 279–281.

[106] Tokmakoff, A. Time-Dependent Quantum Mechanics and Spectroscopy. http://tdqms.uchicago.edu/, Accessed: 07-01-16.

[107] Schatz, G.; Ratner, M. *Quantum Mechanics in Chemistry.*; Dover Books on Chemistry; Dover Publications, 1993.

[108] Petit, A. S.; Subotnik, J. E. *J. Chem. Phys.* **2014**, *141*.

[109] Thomas, M.; Brehm, M.; Fligg, R.; Vohringer, P.; Kirchner, B. *Phys. Chem. Chem. Phys.* **2013**, *15*, 6608–6622.

[110] Lopata, K.; Govind, N. *Journal of Chemical Theory and Computation* **2011**, *7*, 1344–1355, PMID: 26610129.

[111] Martin, R. *Electronic Structure: Basic Theory and Practical Methods.*; Cambridge University Press, 2004.

[112] Fabrocini, A.; Fantoni, S.; Krotscheck, E. *Introduction to Modern Methods of Quantum Many-body Theory and Their Applications.*; Series on advances in quantum many-body theory amd their applications; World Scientific, 2002.

[113] Lenz, W. *Zeits. f. Physik* **1924**, *25*, 299–311.

[114] Sponer, H.; Teller, E. *Rev. Mod. Phys.* **1941**, *13*, 75–170.

[115] Tang, J.; Albrecht, A. C. *J. Chem. Phys.* **1968**, *49*, 1144–1154.

[116] Albrecht, A. C. *J. Chem. Phys.* **1961**, *34*, 1476–1484.

[117] Szymanski, H. *Raman Spectroscopy: Theory and Practice*; Springer US, 1967.

[118] Bruner, A.; LaMaster, D.; Lopata, K. *J. Chem. Theor. Comput.* **2016**, *12*, 3741–3750.

[119] Barron, L. D. *Molecular light scattering and optical activity.*; Cambridge University Press, 2004.

[120] Gross, E. K. U.; Kohn, W. *Phys. Rev. Lett.* **1985**, *55*, 2850–2852.

[121] Stener, M.; Fronzoni, G.; de Simone, M. *Chem. Phys. Lett.* **2003**, *373*, 115–123.

[122] Ray, K.; DeBeer George, S.; Solomon, E. I.; Wieghardt, K.; Neese, F. *Chem. Eur. J.* **2007**, *13*, 2783–2797.

[123] Besley, N. A.; Asmuruf, F. A. *Phys. Chem. Chem. Phys.* **2010**, *12*, 12024–12039.

[124] Lopata, K.; Van Kuiken, B. E.; Khalil, M.; Govind, N. *J. Chem. Theor. Comput.* **2012**, *8*, 3284–3292.

[125] Casida, M. E. In *Recent Advances in Density Functional Methods (Part I)*; Chong, D., Ed.; World Scientific, 1995; pp 155–193.

[126] Stratmann, R. E.; Scuseria, G. E.; Frisch, M. J. *J. Chem. Phys.* **1998**, *109*, 8218–8224.

[127] Dreuw, A.; Head-Gordon, M. *Chem. Rev.* **2005**, *105*, 4009–4037.

[128] Adamo, C.; Jacquemin, D. *Chem. Soc. Rev.* **2013**, *42*, 845–856.

[129] Maitra, N. T. *J. Chem. Phys.* **2016**, *144*, 220901.

[130] Fuks, J. I.; Luo, K.; Sandoval, E. D.; Maitra, N. T. *Phys. Rev. Lett.* **2015**, *114*, 183002.

[131] Provorse, M. R.; Isborn, C. M. *Int. J. Quant. Chem.* **2016**, *116*, 739–749.

[132] Nguyen, T. S.; Koh, J. H.; Lefelhocz, S.; Parkhill, J. *J. Phys. Chem. Lett.* **2016**, *7*, 1590–1595.

[133] Fischer, S. A.; Cramer, C. J.; Govind, N. *J. Chem. Theor. Comput.* **2015**, *11*, 4294–4303.

[134] Prezhdo, O. V.; Duncan, W. R.; Prezhdo, V. V. *Acc. Chem. Res.* **2008**, *41*, 339–348.

[135] Falke, S. M.; Rozzi, C. A.; Brida, D.; Maiuri, M.; Amato, M.; Sommer, E.; De Sio, A.; Rubio, A.; Cerullo, G.; Molinari, E.; Lienau, C. *Science* **2014**, *344*, 1001–1005.

[136] Chapman, C. T.; Liang, W.; Li, X. **2013**, *117*, 2687–2691.

[137] Miyamoto, Y.; Rubio, A.; Tománek, D. *Phys. Rev. Lett.* **2006**, *97*, 126104.

[138] Petrone, A.; Lingerfelt, D. B.; Rega, N.; Li, X. **2014**, *16*, 24457–24465.

[139] Reeves, K. G.; Yao, Y.; Kanai, Y. *Phys. Rev. B* **2016**, *94*, 041108.

[140] Ding, F.; Guidez, E. B.; Aikens, C. M.; Li, X. **2014**, *140*, 244705.

[141] Peng, B.; Lingerfelt, D. B.; Ding, F.; Aikens, C. M.; Li, X. **2015**, *119*, 6421–6427.

[142] Ding, F.; Goings, J. J.; Frisch, M. J.; Li, X. **2014**, *141*, 214111.

[143] Ding, F.; Liang, W.; Chapman, C. T.; Isborn, C. M.; Li, X. **2011**, *135*, 164101.

[144] Skinner, J. L.; Hsu, D. *J. Phys. Chem.* **1986**, *90*, 4931–4938.

[145] Yanai, T.; Tew, D. P.; Handy, N. C. *Chem. Phys. Lett.* **2004**, *393*, 51–57.

[146] Dunning Jr., T. H.; Hay, P. J. In *Methods of Electronic Structure Theory*; Schaefer III, H. F., Ed.; 1977; Vol. 3; pp 1–27.

[147] Hay, P. J.; Wadt, W. R. *J. Chem. Phys.* **1985**, *82*, 270–283.

[148] Chenu, A.; Scholes, G. D. *Annu. Rev. Phys. Chem.* **2015**, *66*, 69–96, PMID: 25493715.

[149] Hayes, D.; Griffin, G. B.; Engel, G. S. *Science* **2013**, *340*, 1431–1434.

[150] Engel, G. S.; Calhoun, T. R.; Read, E. L.; Ahn, T.-K.; Mančal, T.; Cheng, Y.-C.; Blankenship, R. E.; Fleming, G. R. *Nature* **2007**, *446*, 782–786.

[151] DiVincenzo, D. P.; Loss, D. *J. Magn. Magn. Mater.* **1999**, *200*, 202–218.

[152] Swavey, S.; Brewer, K. J. *Inorg. Chem.* **2002**, *41*, 4044–4050.

[153] Mayr, A.; Yu, M. P. Y.; Yam, V. W.-W. *J. Am. Chem. Soc.* **1999**, *121*, 1760–1761.

[154] Brown-Xu, S. E.; Kelley, M. S. J.; Fransted, K. A.; Chakraborty, A.; Schatz, G. C.; Castellano, F. N.; Chen, L. X. *J. Phys. Chem. A* **2016**, *120*, 543–550.

[155] Lockard, J. V.; Rachford, A. A.; Smolentsev, G.; Stickrath, A. B.; Wang, X.; Zhang, X.; Atenkoffer, K.; Jennings, G.; Soldatov, A.; Rheingold, A. L.; Castellano, F. N.; Chen, L. X. *J. Phys. Chem. A* **2010**, *114*, 12780–12787.

[156] Ma, B.; Djurovich, P. I.; Garon, S.; Alleyne, B.; Thompson, M. E. *Adv. Func. Mater.* **2006**, *16*, 2438–2446.

[157] Ma, B.; Li, J.; Djurovich, P. I.; Yousufuddin, M.; Bau, R.; Thompson, M. E. *J. Am. Chem. Soc.* **2005**, *127*, 28–29.

[158] Davydov, A. *Zh. Eksp. Teor. Fiz.* **1948**, *18*, 210–218.

[159] Galli, C.; Wynne, K.; LeCours, S. M.; Therien, M. J.; Hochstrasser, R. M. *Chem. Phys. Lett.* **1993**, *206*, 493–499.

[160] Wynne, K.; Hochstrasser, R. M. *Chem. Phys.* **1993**, *171*, 179–188.

[161] Cohen-Tannoudji, C.; Diu, B.; Laloe, F. *Quantum Mechanics, 2 Volume Set*; Wiley, 1992.

[162] Martin, R. L. *J. Chem. Phys.* **2003**, *118*, 4775–4777.

[163] Ding, F.; Chapman, C. T.; Liang, W.; Li, X. **2012**, *137*, 22A512.

[164] Mulliken, R. S. *J. Am. Chem. Soc.* **1952**, *74*, 811–824.

[165] Hush, N. S. *Prog. Inorg. Chem.*; John Wiley & Sons, Inc., 1967; pp 391–444.

[166] Cave, R. J.; Newton, M. D. *Chem. Phys. Lett.* **1996**, *249*, 15 – 19.

[167] Englman, R.; Jortner, J. *Mol. Phys.* **1970**, *18*, 145–164.

[168] Lingerfelt, D. B.; Lestrange, P. J.; Radler, J. J.; Brown-Xu, S. E.; Kim, P.; Castellano, F. N.; Chen, L. X.; Li, X. **2017**, *121*, 1932–1939.